TITLE:
A Eukaryotic Circuit for Secrete-and-Sense Autonomy

Lingxia Qiao[1†], Amer Ali Abd El-Hafeez[2†¶], I-Chung Lo[2†], Saptarshi Sinha[2], Krishna K. Midde[2], Tony Ngo[3], Nicolas Aznar[2], Inmaculada Lopez-Sanchez[2], Vijay Gupta[2], Marilyn G. Farquhar[2€], Padmini Rangamani[1*] and Pradipta Ghosh[2, 4-6*]

Affiliations:
[1]Department of Mechanical and Aerospace Engineering, Jacob's School of Engineering, University of California San Diego, La Jolla, CA.
[2]Department of Cellular and Molecular Medicine, School of Medicine, University of California San Diego, La Jolla, CA.
[3]Skaggs School of Pharmacy and Pharmaceutical Science, University of California San Diego, La Jolla, CA.
[4]Moores Comprehensive Cancer Center, University of California San Diego.
[5]Department of Medicine, School of Medicine, University of California San Diego, La Jolla, CA.
[6]Veterans Affairs Medical Center, La Jolla, CA.

[†]These authors contributed equally.
[€]Acknowledged posthumously

***Correspondence to:**

Padmini Rangamani, Ph.D.; Professor, Department of Mechanical and Aerospace Engineering, University of California San Diego; 9500 Gilman Drive (MC0411), La Jolla, CA 92093.
Phone: 858-534-4734. Email: prangamani@ucsd.edu

Pradipta Ghosh, M.D.; Professor, Departments of Medicine and Cellular and Molecular Medicine, University of California San Diego; 9500 Gilman Drive (MC 0651), George E. Palade Bldg, Rm 232, 239; La Jolla, CA 92093. Phone: 858-822-7633. Email: prghosh@ucsd.edu

¶ **Secondary Affiliation**: Pharmacology and Experimental Oncology Unit, Cancer Biology Department, National Cancer Institute, Cairo University, Cairo, Egypt

Abbreviations: GIV, Gα-interacting Vesicle-associated protein; GEM, guanine nucleotide exchange modulator; DoRA, dose-response alignment; Arf1, ADP-ribosylation factor-1; EGF, Epidermal growth factor; ER, endoplasmic reticulum; ERGIC, ER-Golgi Intermediate Compartment; CLC, closed loop control; GGA, Golgi-localized, γ-ear-containing, Arf -binding protein.

GRAPHIC ABSTRACT ("A Eukaryotic Circuitry for Secrete-and-Sense Autonomy")

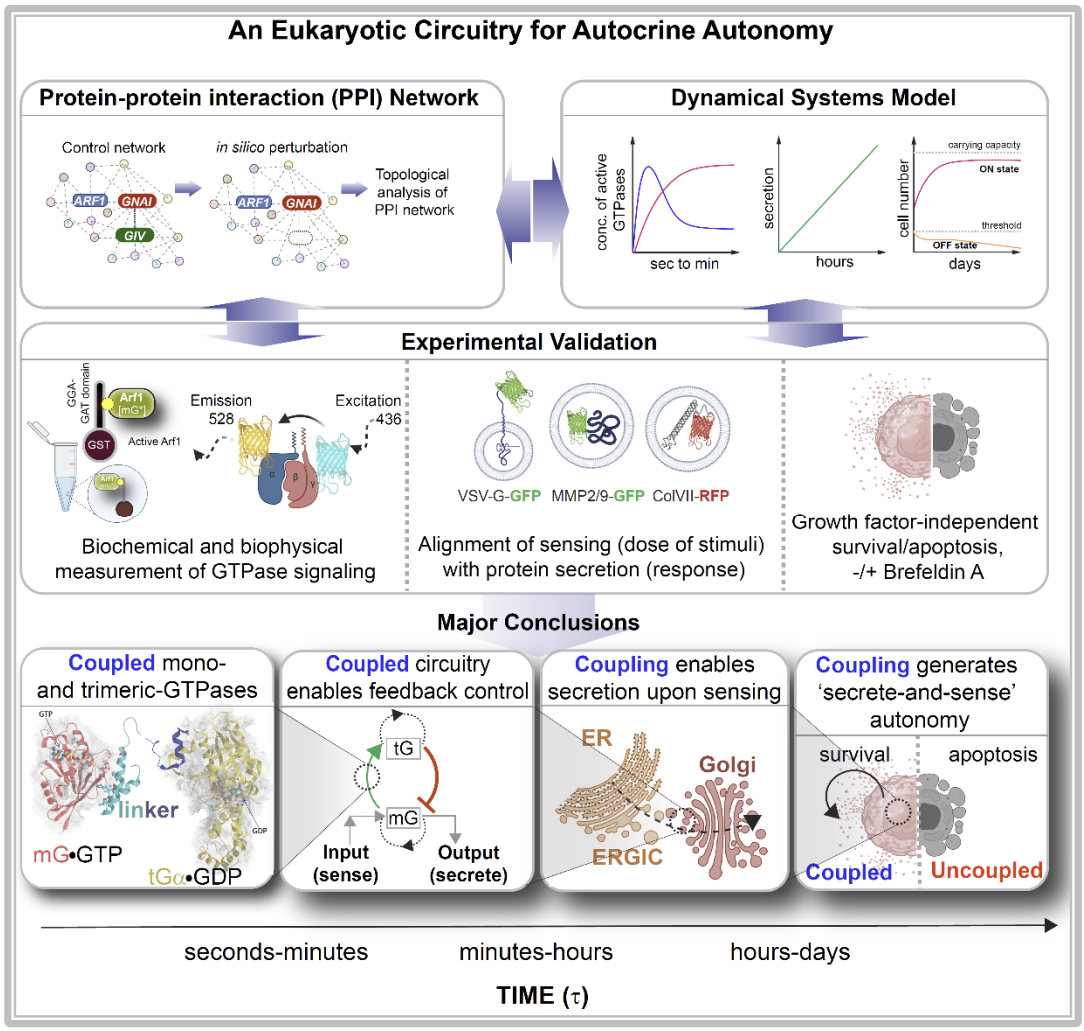

In Brief: This work delivers an experimentally validated dynamical systems model of the cooperativity between two distinct classes of biological switches in eukaryotic cells and reveals the basis of secrete-and-sense autonomy in cancer.

HIGHLIGHTS:

- Modeling and experimental approaches were used to dissect a coupled GTPase circuit
- Coupling enables closed loop feedback and mutual control of GTPases
- Coupling generates dose response alignment behavior of sensing and secretion.
- Coupling is critical for multiscale feedback control to achieve autocrine autonomy.

SUMMARY:

Cancers represent complex autonomous robust systems, displaying interconnectivity with feedback control. Autonomy is fueled by a cancer cell's ability to 'secrete-and-sense': a poorly understood phenomenon. Using an integrated systems and experimental approach, here we dissect the impact of a feedback-coupled GTPase circuit within the secretory pathway that imparts secrete-and-sense autonomy. The circuit is assembled when the Ras-superfamily monomeric GTPase Arf1, and the heterotrimeric GTPase Giαβγ and their corresponding GAPs and GEFs are coupled by the scaffold protein GIV/Girdin, a *bona fide* metastasis-related protein across a variety of solid tumors. One forward and two key negative feedback loops within the circuit create closed-loop control (CLC), allow the two GTPases to coregulate each other, and convert the expected switch-like behavior of Arf1-dependent secretion into an unexpected dose response alignment behavior of sensing and secretion. Such behavior translates into survival that is self-sustained by autocrine secretion. Findings highlight how enhanced coupling of two biological switches in cancer cells is critical for multiscale feedback control to achieve autocrine autonomy.

INTRODUCTION

One of the fundamental hallmarks of all cancers is out-of-control autonomy of cell suvival, proliferation, and invasion [1]. Despite rapid advances in molecular and cell biology, the mechanisms by which cancer cells maintain autonomous growth as they progress through carcinogenesis and acquire their metastatic ability remains widely debated. Autonomous cell survival and replication is an essential feature of malignant tumors and is hypothesized [2] to arise from: (a) auto/paracrine growth stimulation; (b) growth factor receptor abnormalities; (c) abnormal signal transduction; (d) poor fidelity during DNA replication. Of these 4 causes, serum-free cell culture studies squarely implicate autocrine secretion of growth factors as key support for intracellular mechanisms that impart autonomy (reviewed in [2]). Such 'secrete-and-sense' circuits allowing cells to secrete and sense the same signaling molecule are ubiquitous [3]; these autocrine secrete-ans-sense mechanisms don't just enable autonomy [4] but also generate diverse social behaviors, and recur across species [3].

Autocrine secretion of growth factors relies on an essential, efficient, and accurate molecular machinery and a central paradigm of modern cell biology, the secretory pathway, whose importance in physiology and in diseases such as cancers has been established over the past five decades[5,6]. To interact with their environment, mammalian cells produce ~ 2641 soluble proteins (signaling proteins, enzymes, hormones, antibodies, extracellular matrix proteins and structural components) and >5500 membrane proteins [7], all trafficked through the protein secretory pathway. This pathway consists of various modules that are compartmentalized on the endoplasmic reticulum (ER) and the Golgi apparatus and are responsible for folding, processing of the post-translational modifications (PTMs), and trafficking of the proteins routed to the membrane of extracellular space [8,9]. Nearly all these structural components and functional aspects of the secretory pathway have been found to be deregulated in cancers, ranging from observed changes in Golgi shape ('onco-Golgi'[10]), or its structural proteins and the ability to glycosylate cargo proteins[11], which inspired the development of disruptors of this ER-Golgi secretory system as anti-cancer agents[12-17].

Despite these insights, the core mechanisms that impart cell autonomy, i.e., auto/paracrine stimulation, which enables cells to 'secrete-and-sense', remains poorly understood, underexplored, and untapped for both mechanistic understanding and for the development of therapeutics. This work explores one fundamental network motif that contributes to cellular autonomy; using systems biology approaches and explicit integration of experimental biology and computational methods, we assess the impact of perturbing this motif.

RESULTS

An integrated systems and experimental approach to dissect a Golgi-localized GTPase circuit

Here we use a transdisciplinary approach (see legend, **Figure 1**) to dissect the role of an endomembrane GTPase circuit at the Golgi (**Figure 1A**) that dynamically couples two unlikely and distinct species of biological switches that gate signal transduction (**Figure S1A**; **Supplementary Movie 1**) -- small or monomeric (m) and heterotrimeric (t) GTPases. The first evidence for the existence of this circuit emerged in 2015 [18]. Prior to that, mGTPases were mostly believed to function within the cell's interior and were primarily concerned with organelle function and cytoskeletal remodeling [19-21]. tGTPases, on the other hand, were believed to primarily function at the plasma membrane (PM) from where they gate the duration, type and extent of signals that are initiated by receptors on the cell's surface [22]. Using a combination of biochemical, biophysical, structural modeling, live cell imaging, and numerous readouts of Golgi functions, it was shown that the mGTPase Arf1 and the tGTPase Gi co-regulate each other on the Golgi through one key forward reaction [Arrow 1, **Figure S1A-B**; recruitment by active Arf1 of GIV/Girdin (**Figure 1A**; "linker"), a non-receptor guanine-nucleotide exchange factor (GEF) for Gi[23-26] and a set of two feedback loops that culminate in the maximized activation of ArfGAP2/3, which terminates Arf1 signaling (Arrows 2 and 3, **Figure S1A-B**) [18]. This phenomenon of co-regulation between the two classes of GTPases was shown to be critical for maintaining Golgi shape and function at steady states, two closely intertwined processes regulated by Arf1. The triggers for or the consequence(s) of such co-regulation on signal sensing/response remained unknown.

Because coupling of two species of GTPase switches, Arf1 and Gi, with feedback control is likely to generate complex, nonlinear, and non-intuitive emergent properties and, in turn, regulate secretion at the Golgi, we used cross-disciplinary approaches to dissect the role of the coupled GTPases within the secretory pathway (**Figure 1B-C**). We began by developing a dynamical systems model for this coupled circuit, using the general framework presented in [27,28] (**Figure 1B**; see *STAR methods*) and drawing clues from protein-protein interaction (PPI) network analyses, to generate testable hypotheses and validate experimentally (**Figure 1C**). The integrated approach allowed us to connect across time scales of the emergent behavior of the coupled GTPase circuit with cellular secretion, secrete-and-sense autonomy, and cell survival. As for the choice of experimental model system in which to study the consequences of uncoupling the GTPase, we chose two different cancer cell lines, HeLa cervical cancer and MDA-MB231 breast cancer cells. This is because we and others have shown that transcriptional upregulation or post-transcriptional activation [29-31] of GIV (the 'linker' between the two GTPases; **Figure 1A**) supports several sinister tumor cell properties, including, proliferation, invasiveness, stemness, survival, chemoresistance and angiogenesis [32,33]. Consistent with the notion that cell autonomy fuels unrestricted proliferation [2], collective invasiveness [34-37], and adaptability (drug resistance [38]), elevated expression of the GIV linker protein in a variety of solid tumors [33,39], both in primary tumors [40,41] as well as in circulating tumor cells [42,43] have been shown to correlate with tumor aggressiveness and poor survival across cancers. Finally, model and PPI network-driven predictions of uncoupling the GTPases or interrupting secrete-and-sense

autonomy were experimentally validated in the two cancer cell lines in the absence of the GIV linker protein (**Figure 1D**).

EGF activates Arf1 (mG*) at the Golgi and triggers the recruitment of a GEF for trimeric Giα•βγ

We first asked if and how coupling and mutual coregulation impacted the temporal finiteness of either GTPase signaling and/or the alignment of secretory responses to the input signal, i.e., growth factors (**Figure 2A**). For the purposes of modeling, we interrogated key events within the circuit that could be measured/assessed experimentally using available tools and experimental approaches (Arrows 1-3; see legend **Figure 2B;** see *STAR* methods). We also assumed that the finiteness of Arf1 activation-inactivation cycle was a surrogate indicator of successful anterograde cargo movement through the major compartments (i.e., ERGIC to the Golgi) within the secretory pathway. This is because Arf1 regulates membrane traffic through a cycle of GTP binding and hydrolysis [44]-- GTP binding is a pre-requisite for membrane curvature and vesicle formation [45] from the donor compartment, whereas GTP hydrolysis is a pre-requisite for vesicle uncoating [46] and fusion with acceptor compartment. The steps that involve membrane mechanics when converting the Arf1 activity to secretion, were also modeled using Hill-type kinetics to capture the switch-like behavior. All governing equations were modeled using Hill-type equations based on logic operators such that the activity of each species varies between 0 and 1 [47,48].

We began by investigating if and how this circuit of coupled GTPases responds to external stimuli. The stimuli we prioritized in this study is growth factors, and more specifically epidermal growth factor (EGF) because of prior evidence documenting its role in the regulation of Golgi secretion [49], its fragmentation during mitosis [50], and most importantly, in the activation of Arf1 [51-53]. We began by measuring the very first event in the circuit, i.e., the modulation of Arf1 activity by EGF using a previously validated pull-down assay that uses the GST-GAT domain of GGA3 to selectively bind the active GTP-bound pool of Arf1[54] (**Figure 2C**). The levels of Arf1•GTP were increased ~3-fold within 5 min after ligand stimulation, followed by a return to near baseline by 30 min (**Figure 2D-E**). These temporal dynamics of Arf1 activation-inactivation after EGF stimulation were used to fit the parameters for Arf1 activity in the computational model of the circuit (**Figure 2F**) (R2 and normalized RMSE are 0.72 and 0.19 respectively; see *STAR methods* for model parameters). Such fitting completed the characterization of the first GTPase switch, i.e., Arf1; in this case, the input is ligand stimuli (EGF) and the output is Arf1-GTP (OUTPUT #1; mG*).

The immediate and key consequence of Arf1 activity within the coupled GTPase circuit is the first segment of the feed-forward loop, i.e., the recruitment of an effector of mGTPase Arf1 and a guanine nucleotide exchange factor of tGTPase Gi, GIV/Girdin [18] (Arrow 1; **Figure 2B**). An evolutionarily conserved region in the N-terminal Hook domain of GIV bearing semblance to the 'Hook-like patch' on GGA-GAT domain [55-58] was shown to directly and preferentially bind to the active GTP-bound conformation of Arf1 [18]. Because active Arf1 regulates

membrane association of GIV [18] and several proteins are involved in vesicle trafficking [44], we asked if ligand-dependent activation of Arf1 was also associated with the recruitment of GIV. Using immunofluorescence microscopy, we confirmed that membrane-colocalization of Arf1 and GIV was increased within 5 min after ligand stimulation compared to serum-starved control cells (**Figure 2G**). Quantification of the Arf1-positive Golgi regions using a Mander's overlap coefficient (MOC) confirmed that the EGF-induced increase in the degree of colocalization between Arf1-HA and GIV fluorophores was significant (**Figure 2H**). These results indicate that EGF activates mG* at the Golgi, and the latter triggers the recruitment of GIV, which can trigger the activation of trimeric Giα•βγ (**Figure 2I).**

EGF triggers the activation of Gi (tG*) on Golgi membranes

We next evaluated the second segment of the feed-forward loop, i.e., GIV's ability to bind and activate the tGTPase Gi on Golgi membranes (**Figure 3A**). GIV does so using its C-terminal GEM motif, the structural basis for which has now been resolved [59]. To this end, we used a previously well-established FRET-based assay in living cells [60] in which the dissociation of $G\alpha i_1$-YFP and CFP-$G\beta_1\gamma_2$ (low FRET) is used as a surrogate marker for 'activation' of Gi (**Figure 3B**) in cells with/without GIV (**Figure 3C**). Using these constructs in living cells, we previously showed that Gαi1-YFP localized to two major sites, i.e., the Golgi and the PM. While most of the Gαi at the PM stays complexed with Gβγ as inactive heterotrimers, a significant portion of the Golgi-localized pool is found to be dissociated [18]. When serum-starved cells were stimulated with EGF, we found that in cells with GIV (control cells) there was a significant drop in FRET both at the Golgi and at the PM within 5 min after EGF stimulation (**Figure S2A-B**). The extent of drop in FRET in the Golgi region, indicative of trimer dissociation at the Golgi, continued to peak by 15 min, reaching a plateau by 25-30 min after EGF stimulation (**Figure 3D-E**; **Figure S2A-B**). The delay in the activation of tGTPase relative to the mGTPase is consistent with previous observations that propagation of signal from the extracellular space to the cell interior takes longer than PM-proximal events [61]. These experimentally observed dynamics of tGTPase activation at the Golgi (OUTPUT #2) in response to EGF (INPUT) in control cells matched model predictions with excellent fitness (R^2 and normalized RMSE are 0.54 and 0.41 respectively; see *STAR methods* for model parameters). Furthermore, our model predicted that EGF-induced tGTPase activation at the Golgi would be abolished in cells without GIV (shGIV), in which m- and tGTPases cannot be coupled within the circuit (**Figure 3D**). This prediction was experimentally validated in shGIV cells using the same FRET-based approach; the expected drop in FRET in the Golgi region was virtually abolished in these cells (**Figure 3D** *bottom*; **Figure 3F**). Using an anti-Gαi:GTP mAb, which specifically recognizes the GTP-bound active conformation of the Gαi (1/2/3) proteins (**Figure 3G**, *top*) [62], we further confirmed that EGF triggered-active Gαi was detected at the Golgi in control cells, where it colocalized with Man II (**Figure 3G**, *bottom*). Similar findings were seen also with 10% serum (representing a well-mixed growth factor stimuli) and lysophosphatidic acid (LPA), a ligand for the GPCR, LPAR (**Figure S2C-D**). Taken

together, these results demonstrate that Gαi is activated at the Golgi upon EGF stimulation, and that such activation requires the coupling of the two GTPases by GIV.

EGF activates ArfGAP, terminates Arf1 signaling *via* feedback loops within the closed loop system

We next evaluated the feedback loops, which are critical for the 'closed loop' architecture of the circuit, i.e., deactivation of Arf1 (mG*) by ArfGAP2/3 (mGAP) (**Figure 3H**). Two negative feedback loops activate ArfGAP2/3 (arrows 2 and 3 in **Figure 3A**). Arrow 2 represents GIV's ability to bind and recruit ArfGAP2/3 to COPI vesicles and the Golgi membranes. Failure to recruit ArfGAP2/3 in GIV-depleted cells was implicated, in part, to the elevated levels of Arf1•GTP and stalled anterograde secretion in these cells [18]. Arrow 3 represents the fact that GIV suppresses the levels of active Arf1 and regulates ERGIC→Golgi transport and Golgi structure in part *via* activation of Gi and release of 'free' Gβγ; GIV's GEF function (which activates Gαi) is required for this effect [18]. We noted that by design, both negative feedback loops, arrows 2 and 3 depend on the forward reaction, arrow 1, which involves the recruitment of GIV (tGEF) (**Figure 2B**). Using the rate of deactivation of Arf1 after ligand stimulation as a readout, we next measured the activity of ArfGAP2/3 in control and GIV-depleted cells responding to EGF (**Figure 3I**). In parallel, we conducted simulations for the coupled circuit in the absence of either arrows 2 and 3, or when both are lost simultaneously in cells without GIV (**Figure 3J**). Such simulations transform the coupled GTPase switches from a closed loop with negative feedback to an open loop circuit without such feedback [63]. Simulations predicted that in shGIV cells, which lack both negative feedback loops, Arf1 activity after EGF stimulation will be sustained, disrupting the temporal finiteness of this signal (**Figure S2F**; red, **Figure 3K**). These predictions matched experiments closely -- Arf1 activity peaked within 5 min after EGF stimulation and rapidly reduced thereafter by 15 min in control cells but remained sustained until 15 min in GIV-depleted cells (**Figure 3I, S2E-F**). When we conducted simulations after disabling the two negative feedback arrows one at a time, the predicted dynamics of Arf1 activity (OUTPUT #1) in response to EGF (INPUT) mirrored that of having both loops disabled (as in shGIV cells) (**Figure 3J**). These findings suggest the existence of an 'AND gate'-like digital logical operation [64], i.e., a HIGH output (ArfGAP2/3 activity, and resultant termination of Arf1 signaling) results only if both the inputs to the AND gate (arrows 2 and 3) are HIGH. If neither arrow or only one of the arrows (inputs to the AND gate) are HIGH, LOW output results. In signal transduction, such logical operations serve to integrate multiple input signals.

Finally, we sought to estimate the impact of the negative feedback loops on the activity of the tGTPase, Gi (OUTPUT #2) in response to EGF (INPUT). Model simulations predicted that the Gi activity was practically unaffected (maybe even slightly increased) when either negative feedback loop was removed (**Figure 3K**). Because experimental tools/approaches to specifically inhibit one negative feedback loop at a time do not exist at present, experimental validation of these predictions was not feasible. Regardless, these findings suggest that an AND gate of two negative feedback loops exerts the most dramatic effects on the mGTPase (Arf1) and has little or no effect on the activity of the tGTPase.

Coupled GTPases are predicted to enable high fidelity concordant response to EGF

Advantaged with an experimentally validated computational model of a naturally occurring circuit representing an unlikely coupling of two species of GTPases, we next asked how might such coupling be beneficial to cells. More specifically, we asked how coupled (closed loop control) *vs*. uncoupled (open loop) systems impact mono- and trimeric-GTPase signaling on endomembranes and organelle response, i.e., secretory functions of the Golgi in response to stimuli that is perceived at the ectomembrane. As shown in **Figures 1-3**, the temporal propagation of the input signal (EGF) takes ~5 min to trigger events at the Golgi. This is considerably delayed compared to most of the well-defined EGF-stimulated, receptor-proximal events (**Figure 4A**), i.e., receptor dimerization, autophosphorylation, and adaptor recruitment, all of which begin within ~2-5 sec of ligand stimulation, and plateau by 20-30 sec and begin to fade by 80-90 sec [65]. Even the initiation of the downstream MAPK cascade begins by 10-20 sec after ligand stimulation [65]. This delay is consistent with the concept of propagation delay in networks [61], defined as the amount of time it takes for the signal to travel from the sender (i.e., receptor at the PM) to the receiver at the interior of cells (i.e., Arf1 on the Golgi).

To gain insights into how coupling impacts responses to the input signal (EGF), we conducted simulations with the inclusion of noise within the EGF stimuli over a wide range of concentrations and compared the dose-response behavior at steady-states of the different outputs in coupled switches against a single switch (mG/G*). In the case of a single switch, both mGEF and mG* show classic dose-response curves (**Figure 4B**) but lack alignment. By contrast, in the coupled switches, mGEF and mG* both show the classic dose-response curves with increased alignment between mGEF and mG* at higher EGF doses (**Figure 4C**). The misalignment in the case of single switch is evident in plots of fractional activation of mG* for a given mGEF activity; a single Arf1 switch displays hyperresponsiveness, in that, max mG* is achieved even with minimal mGEF activity (**Figure 4D**). In the case of coupled switches, similar plots of fractional activation of mG* for a given mGEF activity show dose-response alignment with an unexpected linear relationship (**Figure 4E**). Although unexpected for a GTPase switch, this finding is consistent with what is generally expected in a closed loop with negative feedback control [63]. To further validate this finding, we also compared these input-output relationships in the presence of intracellular noise [simulated within the concentrations of the different species (nodes) and the connections between them (arrows)] (see **Supplementary Online Materials** for details). For the single switch, the mGEF-mG* relationship displayed a Hill coefficient of 1.37 (**Figure 4F**), and the shape of the curve is similar to that when noise is only within the EGF stimulus; the mGEF-mG* relationship (switch #1) in the coupled switches continued to display a similar linear response (**Figure 4G**) as Figure 4E. Besides, the EGF-tG* relationship shows a Hill coefficient of 1.73 (**Figure 4H**), and the tGEF→tG* switch (switch #2) shows a dose-response behavior close to the saturation regime of an ultrasensitive curve (n_{Hill}=3.82) (**Figure 4I**). These findings indicate that the information propagation via the closed loop coupled system appears to be robust to noise in the stimulus, noise in the concentrations of the species, and noise in the connections[66].

Coupled GTPases are predicted to support secrete-and-sense autonomy and cell number

To better understand the impact of uncoupling of the GTPase circuit on Arf1-dependent secretory functions of the Golgi, we conducted two distinct analyses: (i) protein-protein interaction (PPI) network analysis and (ii) dynamical systems modeling.

To restrict the PPI network analysis to the Golgi, we first extracted a Golgi-annotated subcellular localization network of high confidence GIV and Arf1 correlators, based on a proximity-dependent biotinylation map of a human cell[67] (**Figure 5A**). As anticipated, the list of proteins in such a Golgi-restricted interactome was enriched for cellular processes that are normally dependent on the secretory pathway, e.g., intracellular transport, post-Golgi vesicle transport, viral processes, localization of proteins to the cell periphery and the regulation of GTPases (**Figure 5B**; **Figure S3A**). However, there was also an enrichment of pathways that are not typically or directly attributed to the secretory pathway, e.g., assembly and organization of cell junctions and the establishment and maintenance of cell polarity, organization of mitotic spindle and the actin cytoskeleton and growth factor signaling (**Figure 5B**; **Figure S3A**). Next the list of Golgi-localized proteins was expanded by incorporating the GIV interactors from BioGRID[68] (**Figure S3B**). *In silico* uncoupling of the Arf1●GIV●Gi coupling at the Golgi (by removal of GIV from the network; **Figure S3C**) was followed by the most basic assessment of network connectivity of Arf1, i.e., shortest path analysis and pathways represented by the most frequently encountered end proteins of those paths (see workflow in **Figure 5C;** and *STAR methods*). We found that paths from Arf1 to several nodes within the network were impacted (**Figure S3C-D**). The end proteins (i.e., nodes) which share a striking set of three themes: “sensing” of diverse ligands/stimuli, e.g., growth factors, peptide and steroid hormones, cytokines (yellow nodes in **Figure 5D**), “secreting” proteins to the extracellular space (red nodes in **Figure 5D**) and “survival” signaling via the PI3K-Akt pathways (teal nodes in **Figure 5D**). As anticipated in the absence of GIV, Gi and second messenger signaling were predicted to be impacted (blue nodes in **Figure 5D**). Cellular homeostasis and cell number were also predicted to be impaired (green nodes in **Figure 5D**). These findings show that uncoupling of the Golgi-localized GTPase circuit may impact some far-reaching functions of Arf1 in the secretory pathway, among which is secretion that may be critical for sensing (the autocrine ‘secrete-and-sense’ loop) that supports the maintenance of cell number, via balanced proliferation, survival, and death, may be key.

We next used systems modeling approaches to interrogate how coupled (closed loop control) *vs*. uncoupled (open loop) GTPase systems at the Golgi impact cargo secretion in response to stimuli. Because cargo movement within the secretory pathway requires cyclical activation-inactivation of Arf1[44,45], we used a set of logic-based differential equations (**Figure 6A**) to couple the activation-inactivation cycles of Arf1 to secretion. Our model predicted that the secretion function shows an ultrasensitive response (n_{Hill}=1.86) as a function of the stimulus (i.e., a given dose of EGF) when the two GTPase switches are coupled; in the absence of coupling, we predict a reduced response (**Figure 6B**). Intriguingly, secretion function in the coupled state shows a dose-response alignment with Gi activity (tG*; **Figure 6C**).

Based on published models[69-71] of secretion-dependent cell survival, and our PPI analysis (**Figure 5D**), we next modeled cell number as the final readout; cell number was modeled based on previous work by Alon and his colleagues[70]. However, unlike m/tG* activity assays (which happen in sec to min) and cell secretion (which may begin within min but is measured in hours), their impact on cell number, which reflects homeostatic balance between cell proliferation, survival and death requires a longer time scale (several hours and even, days). Because acute EGF stimulation reaches a quasi-steady state within ~ 60 min[72], we asked how the model performs for any generic stimuli, such as varying concentration of serum. The contrasting patterns of secretion as a function of stimulus in coupled and uncoupled switches was also reproduced when the stimulus was calculated as a fraction of max (**Figure 6D**). Our model predicted that when the switches are coupled, the cell number is higher for the coupled versus the uncoupled cells (**Figure 6E and Figure S4**). To specifically analyze the impact of secrete-and-sense autocrine autonomy, we carried out the simulations under restrictive growth conditions, i.e., low/no external stimuli so that cells depend on sensing the molecules it secretes. These simulations under restrictive growth conditions revealed that cells with coupled switches display a higher cell number compared to the cells with uncoupled switches only when the secrete-and-sense loop is highly efficient; this advantage is lost if the loop is abolished (**Figure 6F**). That coupling of GTPases is required for maintaining cell numbers was reproduced using EGF as stimuli (**Figure 6G**), providing continuity with prior model-derived predictions. We also confirmed that the system and the conclusions are robust to noise that is introduced either in stimuli alone, or simultaneously with connections or species (**Figure 6B, C, G**).

GTPase coupling by GIV is required for time and dose-dependent secretion of diverse cargo proteins

We next sought to experimentally validate the predictions from the PPI networkand dynamical systems modeling. First, we examined time-dependent secretion of various types of cargo proteins (**Figure 7A**). We studied the transmembrane cargo protein vesicular stomatitis virus G protein (VSVG) using the well-characterized GFP-tagged VSVG-tsO45 mutant [73]. This mutant VSVG is retained in the ER at 40°C, accumulates in Golgi stacks at 20°C temperature block, from where it escapes to the PM at permissive 32°C (**Figure S5A**). Immunofluorescence studies were carried out in non-permeabilized cells using an anti-VSVG ectodomain antibody to selectively visualize the fraction of molecules that reached the cell surface; the intensity of GFP signals was used towards quantifying the total cellular pool of VSV-G protein. Considerable VSVG accumulated in the Golgi region in both control and GIV-depleted cells under serum starved conditions at 20°C. EGF or serum stimulation was permissive to transport of the VSV-G protein to the PM in control cells at 32°C, but such transport was significantly diminished in GIV-depleted cells (**Figure S5B-C**). Similar results were observed also in the case of EGF-stimulated secretion of three separate soluble cargo proteins, MMP2, MM9 (**Figure S5D-F**) and Collagen (**Figure S5G-H**); these cargo proteins were chosen because of GIV's published role in ECM degradation during cancer metastasis [74] and tissue fibrosis [75]. Together, these findings show that when GIV-

dependent coupling of Arf1•GTP with Gi is lost, the secretory function of the Golgi shows a blunted response to growth factors in the case of all the three cargo proteins analyzed (summarized in **Figure 7A**).

We next asked if the DoRA predicted earlier in the case of Arf1 activity (**Figure 4E**) translates into a similar alignment in the case of cell secretion, and whether uncoupling the GTPases disrupts such dose-responsive secretion. We analyzed the efficiency of secretion of one of the 3 cargo proteins, MMP9, from control and GIV-depleted cells responding to a range of EGF concentrations or 24 h (**Figure 7B**). Quantitative immunoblotting confirmed that dose-dependent secretion was observed in the case of control cells (coupled GTPases) but not in GIV-depleted cells (uncoupled GTPases) (**Figure 7B; 7C** *left*). We conclude that DoRA of Arf1 activity indeed translates into DoRA of cell secretion in cells with coupled GTPases; by contrast, a mis-aligned Arf1 activity (hyper-responsive; **Figure 4D, 7C**, right) translates into a misaligned (hypo-responsive; **Figure 7C**, right).

GTPase coupling by GIV is required for cell survival that relies upon autocrine secretion.

Finally, we t sought to validate the predicted impact of uncoupling the GTPase circuit on cell number. We analyzed the total number of metabolically active cells, as determined by MTT assays, that survive in serum-free conditions or in the presence of increasing concentrations of serum (ranging from 0.25 – 10%) (**Figure 7D***, left*). We found that the number of cells in serum-free or low-serum conditions was significantly higher in the presence of GIV (parental HeLa cells; coupled) than in the absence of GIV (GIV KO cells; uncoupled) (**Figure 7D**); this survival advantage was abolished at higher serum concentrations (see 10% FBS, **Figure 7D**). Reduced cell number in cells without GIV was associated with a concomitant increase in apoptosis and necrosis in the low/no serum conditions (**Figure 7E, S6A-C**), confirming reduced cell survival is, in part, the reason for the low cell numbers observed. We then sought to validate the results of the simulations in growth-restrictive conditions which showed that interrupting the coupled GTPase circuit at the Golgi will reduce cell numbers (**Figure 6F**). We analyzed the number of metabolically active cells in cells with (coupled) or without GIV (uncoupled) across a range of serum conditions and varying concentrations of the mycotoxin Brefeldin A (BFA), a well-known tool to inhibit secretion via its ability to inhibit Arf1 activation [76] (**Figure 7F**). We observed 3 things: (i) as seen in **Figure 7D**, cells with coupled circuit have a significant survival advantage in serum-restricted conditions (see 0 - 2.0% FBS; **Figure 7G**); (ii) that advantage depends on sensing what the cells secrete, because blocking secretion with BFA also eliminates such advantage (**Figure 7H**); (iii) survival in the presence of serum (5-10%) is similar for both “coupled” and “uncoupled” cells, implying non-secreting cells with uncoupled circuits can survive if they can "sense” stimuli that they did not generate (e.g., serum ~5-10% range; **Figure 7G**).

To overcome the limitation of using a single model cell line (i.e., HeLa), we generated a second model, GIV-depleted MDA MB-231 cells (by CRISPR, see *STAR methods*) and sought to reproduce key findings (**Figure 7I-K**). As in the case of HeLa cells, the survival advantage of MDA MB-231 cells with coupled circuit (with GIV, Parental cells) over those with uncoupled circuit (GIV KO) was observed exclusively in low/no serum conditions (see 0 - 2.0% FBS; **Figure 7I**) and blocking secretion with BFA eliminates such advantage (**Figure 7J**). Reduced

cell survival in cells without GIV (uncoupled state) was associated with higher early and later apoptosis and necrosis (**Figure S6D-H**).

These findings show that the coupled GTPase circuit is required for cell survival that is supported exclusively by autocrine secretion (i.e., independent of external growth factors), and by that token, essential for a functional autocrine 'secrete-and-sense' loop (**Figure 7L,** *top*). Interrupting the coupled GTPase circuit at the Golgi appears to disrupt the 'secrete and sense' loop and abrogate cell survival that is supported by such secretion (**Figure 7L,** *bottom*). Because 'secrete-and-sense' loop is a key feature of cellular autonomy [3,4], taken together our findings show that the coupled GTPase circuit in the cell's secretory pathway may be critical for autocrine autonomy.

DISCUSSION

The major discovery we report here is the creation of an experimentally validated multi-timescale model for cell autonomy. We not only formally define the molecular basis for such autonomy (i.e., coupled GTPases in a closed loop circuit at the Golgi), but also demonstrate the consequences when it is manipulated/perturbed. The insights and models derived from this study refine and/or challenge the existing knowledge and spur new paradigms in at least three fields, i.e., of signal transduction, cell secretion, and cancer cell biology in the following ways.

When it comes to the field of signal transduction, emergent properties of ectomembrane signaling circuits at the PM have been identified using systems biology; however, none thus far have coupled the events at the ectomembrane to the events in the cell's interior, i.e., the endomembrane of organelles. Our study experimentally validated a Golgi-localized natural coupling between the two GTPase switches with exquisite feedback control that enables linear activation of Arf1 in response to EGF, which in turn enables the Golgi to mount a response (protein secretion) that is proportionate to the stimuli (sensed at the PM) and robust to noise. The model reveals three notable features -- first, it is noteworthy that both PM-proximal events as well as the endomembrane (Golgi)-localized events peak simultaneously at ~5 min post EGF stimulation, e.g., EGF-triggered pERK [77,78], coupling of ligand-activated EGFR to trimeric Gi at the PM [79], and Golgi localized events such as Arf1 activation. The virtual lack of latency between when these peak signals are reached implies that the cell's network is able to carry out near simultaneous conversations at the ecto(PM)- and the Golgi membranes, and perhaps reflects more responsiveness of the network so that the Golgi membranes can mount a rapid response to the events at the PM. Second, our findings show that the closed loop control system generated DoRA, enabling a linear increase in Arf1/mG* activation and protein secretion. Such DoRA has been described in several major receptor initiated signaling cascades at the PM (from the pheromone response system in yeast to the Wnt→βCatenin, TGFβ→SMAD2/3 and EGFR→MAPK cascades in mammals) [80], but never in endomembrane GTPases. Because a linear DoRA maximally preserves any information during its propagation, and many different cellular signaling systems avoid losing information by transmitting it in a linear manner [81], we conclude that one of the major discernible consequences of the closed loop coupling of two GTPases is its ability to faithfully transmit information from the PM to the Golgi for the latter to mount a concordant secretory response. Third, although the first switch, i.e., Arf1/mG* showed a linear response, each of the subsequent switches (switch #2 and the step of membrane mechanics leading to secretion) becomes progressively ultrasensitive. The net result of this is that the closed loop feedback control allows for a tighter alignment of secretion with respect to EGF by 'stretching' out the dose-response curve across series of switches to propagate the signal from the extracellular space to the interior of the cell. Because the stability behavior of a mathematically simpler version of this closed loop system of coupled GTPases showed that coupling afforded a wide range of steady states [82], it is tempting to speculate that the coupled system allows flexibility in responses over a wide range of stimuli.

When it comes to the field of protein secretion, the cell's secretory pathway was originally believed to be a constitutive function that is regulated by 'housekeeping' genes/proteins that maintain the integrity of the local (membrane or lumenal) environment [83]; however, more recently, that notion has begun to change. For example, an unbiased analysis of the genes that regulate the secretory pathway in diverse tissues indicated that the pathway is responsive to tissue-specific context and extracellular cues [84]. Furthermore, others have shown that tyrosine phosphorylation and dephosphorylation cascades may be important for budding of vesicles from the ER, ERGIC and the Golgi [85]. The only concrete evidence that secretion is regulated by exogenous growth factors emerged in 2008 when the phosphoinositide phosphatase SAC1 was implicated as a 'brake' in anterograde Golgi secretion that is released by growth factors [49]. Thus, although the molecular biology and biochemistry of the secretory pathway are well-studied for its core components [86-88], what remained unknown was how the secretory system (or any intracellular organelle/system) responds proportionately to the external cues. The functional consequences of an endomembrane coupled GTPase system we dissected here fills that knowledge gap. We show that coupling of m/tGTPases with closed loop control within cells is critical to set up feedback controls in yet another scale, i.e., cell secretion and cell fate (i.e., survival *vs*. death).

Finally, when it comes to the field of cancer cell biology, it is well accepted that cancers are deadly because tumor cells display indomitable survival skills despite starvation, genetic mishaps, hypoxia, immune predation, and therapy[1,89]. Our finding that the 'secrete-and-sense' circuit in cells support cancer cell survival has a three-fold impact-- First, although there are existing theories linking secrete-and-sense genetic circuits to cellular autonomy, and the degrees of autonomy and collectiveness are quantifiable and tunable[3,4,90,91, 92], none of them have been studied in the eukaryotic cell. Validation of *in silico* perturbations has not been possible because of lack of mechanistic insights. In dissecting the behavior of the coupled GTPase system, and revealing the consequences of its disruption, both *in silico* and in two different cancer cells, we fill that knowledge gap. Second, intratumoral cellular heterogeneity is known to give rise to an ecosystem of clonal interactions[93,94] that can drive tumor growth, therapeutic resistance, and progression[95-98]. Therefore, it is possible that a few autonomous secretor clones with an intact secrete-and-sense loop could be sufficient to support the survival of neighboring non-secretor clones. If so, uncoupling the GTPases and disrupting the secrete-and-sense autonomy could serve as an impactful therapeutic strategy. Finally, the evolutionary significance of our findings is noteworthy. For example, the linker between the GTPases, i.e., GIV, evolved later in multicellular organisms such as worms[99] and flies[100-103]. GIV's HOOK module (binds mGTPase) evolved in worms and flies[100-103]; its GEM module (binds tGTPases) evolved later in fish[104] and remains to date. Thus, the coupled GTPase circuit likely evolved in higher eukaryotes. This is consistent with the fact that evolution appears to favor efficient signaling circuits that can accomplish many different tasks[105,106]. Because GIV is overexpressed in the most aggressive tumor cells, it is likely that the GTPase coupled circuit is more frequently assembled in those cells. If

so, the circuit may represent an evolutionary masterpiece of multiscale feedback control to achieve autonomy, adaptability, and flexibility.

LIMITATIONS OF THE STUDY

There are three notable limitations. First, the multi-timescale model we built, ignores the spatial aspects of the various feedback control loops. Inclusion of spatial information is expected to provide valuable insights into how an endomembrane-localized circuit may coordinate another layer of feedback control, i.e., secretion-coupled-sensing, from the ectomembrane, i.e., PM. Because the spatial organization of signaling motifs will influence their temporal behaviors, we anticipate the need for further refinement of the current model. Second, by depleting GIV, we disconnect the GTPases and dismantle the entire circuit; a more refined approach that involves the selective disruption of various connections within the circuit could not be attempted because we lack the experimental tools or knowhow for how to achieve such selectivity. Finally, although we studied four different cargo proteins (VSV-G, MMP2/9 and Col-VII) and two types of stimuli (EGF and serum), a more comprehensive assessment of the cell's secretome was not attempted; such efforts could reveal the wider impact of the secrete-and-sense autonomy. Our PPI network analysis predicts that disrupting the coupled GTPase circuit broadly and widely impacts almost all classes of receptors/ligands, and an equally wide array of secreted cargoes. Secretome studies will not only help validate/refute these predictions, but also reveal how the intracellular GTPase circuit controls the composition of the extracellular space.

REFERENCES CITED

1. Hanahan, D. & Weinberg, R.A. The hallmarks of cancer. *Cell* **100**, 57-70 (2000).
2. Chigira, M., Noda, K. & Watanabe, H. Autonomy in tumor cell proliferation. *Med Hypotheses* **32**, 249-254 (1990).
3. Youk, H. & Lim, W.A. Secreting and sensing the same molecule allows cells to achieve versatile social behaviors. *Science* **343**, 1242782 (2014).
4. Maire, T. & Youk, H. Molecular-Level Tuning of Cellular Autonomy Controls the Collective Behaviors of Cell Populations. *Cell Syst* **1**, 349-360 (2015).
5. Matlin, K.S. & Caplan, M.J. The secretory pathway at 50: a golden anniversary for some momentous grains of silver. *Molecular Biology of the Cell* **28**, 229-232 (2017).
6. Trombetta, E.S. & Parodi, A.J. Quality Control and Protein Folding in the Secretory Pathway. *Annual Review of Cell and Developmental Biology* **19**, 649-676 (2003).
7. Uhlén, M.*, et al.* Tissue-based map of the human proteome. *Science* **347**(2015).
8. Rothman, J.E. & Orci, L. Molecular dissection of the secretory pathway. *Nature* **355**, 409-415 (1992).
9. Kelly, R.B. Pathways of protein secretion in eukaryotes. *Science* **230**, 25-32 (1985).
10. Petrosyan, A. Onco-Golgi: Is Fragmentation a Gate to Cancer Progression? *Biochem Mol Biol J* **1**(2015).
11. Zhang, X. Alterations of Golgi Structural Proteins and Glycosylation Defects in Cancer. *Frontiers in Cell and Developmental Biology* **9**(2021).
12. Luchsinger, C., Aguilar, M., Burgos, P.V., Ehrenfeld, P. & Mardones, G.A. Functional disruption of the Golgi apparatus protein ARF1 sensitizes MDA-MB-231 breast cancer cells to the antitumor drugs Actinomycin D and Vinblastine through ERK and AKT signaling. *PLOS ONE* **13**, e0195401 (2018).
13. Núñez-Olvera, S.I.*, et al.* A novel protective role for microRNA-3135b in Golgi apparatus fragmentation induced by chemotherapy via GOLPH3/AKT1/mTOR axis in colorectal cancer cells. *Scientific Reports* **10**, 10555 (2020).
14. Ohashi, Y.*, et al.* AMF-26, a Novel Inhibitor of the Golgi System, Targeting ADP-ribosylation Factor 1 (Arf1) with Potential for Cancer Therapy. *Journal of Biological Chemistry* **287**, 3885-3897 (2012).
15. Ohashi, Y.*, et al.* M-COPA, a Golgi Disruptor, Inhibits Cell Surface Expression of MET Protein and Exhibits Antitumor Activity against MET-Addicted Gastric Cancers. *Cancer Research* **76**, 3895 (2016).
16. Ohashi, Y.*, et al.* Targeting the Golgi apparatus to overcome acquired resistance of non-small cell lung cancer cells to EGFR tyrosine kinase inhibitors. *Oncotarget; Vol 9, No 2* (2017).
17. Wlodkowic, D., Skommer, J., McGuinness, D., Hillier, C. & Darzynkiewicz, Z. ER-Golgi network--a future target for anti-cancer therapy. *Leuk Res* **33**, 1440-1447 (2009).
18. Lo, I.-C.*, et al.* Activation of Gαi at the Golgi by GIV/Girdin imposes finiteness in Arf1 signaling. *Developmental cell* **33**, 189-203 (2015).
19. Evers, E.E., van der Kammen, R.A., Jean, P. & Collard, J.G. Rho-like GTPases in tumor cell invasion. *Methods in enzymology* **325**, 403-415 (2000).
20. Etienne-Manneville, S. & Hall, A. Rho GTPases in cell biology. *Nature* **420**, 629-635 (2002).
21. Takai, Y., Sasaki, T. & Matozaki, T. Small GTP-binding proteins. *Physiological reviews* **81**, 153-208 (2001).
22. Gilman, A.G. G proteins: transducers of receptor-generated signals. *Annual review of biochemistry* **56**, 615-649 (1987).
23. Garcia-Marcos, M., Ghosh, P. & Farquhar, M.G. GIV is a nonreceptor GEF for Gαi with a unique motif that regulates Akt signaling. *Proceedings of the National Academy of Sciences* **106**, 3178 (2009).
24. Kalogriopoulos, N.A.*, et al.* Structural basis for GPCR-independent activation of heterotrimeric Gi proteins. *Proceedings of the National Academy of Sciences* **116**, 16394 (2019).
25. Aznar, N., Kalogriopoulos, N., Midde, K.K. & Ghosh, P. Heterotrimeric G protein signaling via GIV/Girdin: Breaking the rules of engagement, space, and time. *Bioessays* **38**, 379-393 (2016).
26. Ghosh, P. & Garcia-Marcos, M. Do All Roads Lead to Rome in G-Protein Activation? *Trends in Biochemical Sciences* **45**, 182-184 (2020).
27. Cao, S.*, et al.* Quantification of model and data uncertainty in a network analysis of cardiac myocyte mechanosignalling. *Philosophical Transactions of the Royal Society A* **378**, 20190336 (2020).

28. Saucerman, J.J. & McCulloch, A.D. Mechanistic systems models of cell signaling networks: a case study of myocyte adrenergic regulation. *Progress in biophysics and molecular biology* **85**, 261-278 (2004).
29. Dunkel, Y.*, et al.* STAT3 Protein Up-regulates Gα-interacting Vesicle-associated Protein (GIV)/Girdin Expression, and GIV Enhances STAT3 Activation in a Positive Feedback Loop during Wound Healing and Tumor Invasion/Metastasis. *J Biol Chem* **287**, 41667-41683 (2012).
30. Sasaki, K., Kakuwa, T., Akimoto, K., Koga, H. & Ohno, S. Regulation of epithelial cell polarity by PAR-3 depends on Girdin transcription and Girdin-Galphai3 signaling. *J Cell Sci* (2015).
31. Bhandari, D.*, et al.* Cyclin-dependent kinase 5 activates guanine nucleotide exchange factor GIV/Girdin to orchestrate migration–proliferation dichotomy. *Proceedings of the National Academy of Sciences* **112**, E4874-E4883 (2015).
32. Aznar, N., Kalogriopoulos, N., Midde, K.K. & Ghosh, P. Heterotrimeric G protein signaling via GIV/Girdin: Breaking the rules of engagement, space, and time. *Bioessays* **38**, 379-393 (2016).
33. Garcia-Marcos, M., Ghosh, P. & Farquhar, M.G. GIV/ Girdin transmits signals from multiple receptors by triggering trimeric G protein activation. *The Journal of biological chemistry* (2015).
34. Collins, T.A., Yeoman, B.M. & Katira, P. To lead or to herd: optimal strategies for 3D collective migration of cell clusters. *Biomech Model Mechanobiol* **19**, 1551-1564 (2020).
35. Enomoto, M.*, et al.* Autonomous regulation of osteosarcoma cell invasiveness by Wnt5a/Ror2 signaling. *Oncogene* **28**, 3197-3208 (2009).
36. Kopfstein, L. & Christofori, G. Metastasis: cell-autonomous mechanisms versus contributions by the tumor microenvironment. *Cell Mol Life Sci* **63**, 449-468 (2006).
37. Thomas, S.K., Lee, J. & Beatty, G.L. Paracrine and cell autonomous signalling in pancreatic cancer progression and metastasis. *EBioMedicine* **53**, 102662 (2020).
38. Israel, L. Accelerated genetic destabilization and dormancy: two distinct causes of resistance in metastatic cells; clinical magnitude, therapeutic approaches. *Clin Exp Metastasis* **8**, 1-11 (1990).
39. Getz, M., Swanson, L., Sahoo, D., Ghosh, P., and Rangamani, P. Guanine-nucleotide exchange modulator, GIV/Girdin, serves as a tunable valve for growth factor-stimulated cyclic AMP signals *In Revision, Nature Comm. [BioRxiv* ***preprint*** *listed at DOI]* (2017).
40. Ghosh, P.*, et al.* Girdin (GIV) Expression as a Prognostic Marker of Recurrence in Mismatch Repair-Proficient Stage II Colon Cancer. *Clin Cancer Res* (2016).
41. Ghosh, P. Heterotrimeric G proteins as emerging targets for network based therapy in cancer: End of a long futile campaign striking heads of a Hydra. *Aging (Albany NY)* **7**, 469-474 (2015).
42. Barbazan, J.*, et al.* Prognostic Impact of Modulators of G proteins in Circulating Tumor Cells from Patients with Metastatic Colorectal Cancer. *Scientific Reports* **6**, 22112 (2016).
43. Dunkel, Y.*, et al.* Prognostic Relevance of CCDC88C (Daple) Transcripts in the Peripheral Blood of Patients with Cutaneous Melanoma. *Sci Rep* **8**, 18036 (2018).
44. Donaldson, J.G. & Jackson, C.L. ARF family G proteins and their regulators: roles in membrane transport, development and disease. *Nature reviews Molecular cell biology* **12**, 362-375 (2011).
45. Beck, R.*, et al.* Membrane curvature induced by Arf1-GTP is essential for vesicle formation. *Proceedings of the National Academy of Sciences* **105**, 11731-11736 (2008).
46. Tanigawa, G.*, et al.* Hydrolysis of bound GTP by ARF protein triggers uncoating of Golgi-derived COP-coated vesicles. *The Journal of cell biology* **123**, 1365-1371 (1993).
47. Kraeutler, M.J., Soltis, A.R. & Saucerman, J.J. Modeling cardiac β-adrenergic signaling with normalized-Hill differential equations: comparison with a biochemical model. *BMC systems biology* **4**, 1-12 (2010).
48. Tan, P.M., Buchholz, K.S., Omens, J.H., McCulloch, A.D. & Saucerman, J.J. Predictive model identifies key network regulators of cardiomyocyte mechano-signaling. *PLoS Computational Biology* **13**, e1005854 (2017).
49. Blagoveshchenskaya, A.*, et al.* Integration of Golgi trafficking and growth factor signaling by the lipid phosphatase SAC1. *The Journal of cell biology* **180**, 803-812 (2008).
50. Shaul, Y.D. & Seger, R. ERK1c regulates Golgi fragmentation during mitosis. *The Journal of cell biology* **172**, 885-897 (2006).

51. Boulay, P.-L., Cotton, M., Melançon, P. & Claing, A. ADP-ribosylation factor 1 controls the activation of the phosphatidylinositol 3-kinase pathway to regulate epidermal growth factor-dependent growth and migration of breast cancer cells. *Journal of Biological Chemistry* **283**, 36425-36434 (2008).
52. Haines, E., Schlienger, S. & Claing, A. The small GTPase ADP-Ribosylation Factor 1 mediates the sensitivity of triple negative breast cancer cells to EGFR tyrosine kinase inhibitors. *Cancer biology & therapy* **16**, 1535-1547 (2015).
53. Haines, E., Saucier, C. & Claing, A. The adaptor proteins p66Shc and Grb2 regulate the activation of the GTPases ARF1 and ARF6 in invasive breast cancer cells. *Journal of Biological Chemistry* **289**, 5687-5703 (2014).
54. Cohen, L.A. & Donaldson, J.G. Analysis of Arf GTP‐binding protein function in cells. *Current protocols in cell biology* **48**, 14.12. 11-14.12. 17 (2010).
55. Collins, B.M., Watson, P.J. & Owen, D.J. The structure of the GGA1-GAT domain reveals the molecular basis for ARF binding and membrane association of GGAs. *Developmental cell* **4**, 321-332 (2003).
56. Shiba, Y.*, et al.* GAT (GGA and Tom1) domain responsible for ubiquitin binding and ubiquitination. *Journal of Biological Chemistry* **279**, 7105-7111 (2004).
57. Shiba, T.*, et al.* Molecular mechanism of membrane recruitment of GGA by ARF in lysosomal protein transport. *Nature structural biology* **10**, 386-393 (2003).
58. Collins, B.M., Watson, P.J. & Owen, D.J. The structure of the GGA1-GAT domain reveals the molecular basis for ARF binding and membrane association of GGAs. *Developmental cell* **4**, 321-332 (2003).
59. Kalogriopoulos, N.A.*, et al.* Structural basis for GPCR-independent activation of heterotrimeric Gi proteins. *Proceedings of the National Academy of Sciences* **116**, 16394-16403 (2019).
60. Gibson, S.K. & Gilman, A.G. Giα and Gβ subunits both define selectivity of G protein activation by α2-adrenergic receptors. *Proceedings of the National Academy of Sciences* **103**, 212-217 (2006).
61. Brent, R. Cell signaling: what is the signal and what information does it carry? *FEBS letters* **583**, 4019-4024 (2009).
62. Lane, J.R.*, et al.* Antibodies that identify only the active conformation of G(i) family G protein alpha subunits. *FASEB J* **22**, 1924-1932 (2008).
63. Åström, K.J. & Murray, R.M. *Feedback systems: an introduction for scientists and engineers*, (Princeton university press, 2021).
64. Kime, C.R. & Mano, M.M. *Logic and computer design fundamentals*, (Prentice Hall, 2003).
65. Reddy, R.J.*, et al.* Early signaling dynamics of the epidermal growth factor receptor. *Proceedings of the National Academy of Sciences* **113**, 3114-3119 (2016).
66. Uda, S.*, et al.* Robustness and compensation of information transmission of signaling pathways. *Science* **341**, 558-561 (2013).
67. Go, C.D.*, et al.* A proximity-dependent biotinylation map of a human cell. *Nature* (2021).
68. Oughtred, R.*, et al.* The BioGRID database: A comprehensive biomedical resource of curated protein, genetic, and chemical interactions. *Protein Sci* **30**, 187-200 (2021).
69. Hart, Y., Antebi, Y.E., Mayo, A.E., Friedman, N. & Alon, U. Design principles of cell circuits with paradoxical components. *Proc Natl Acad Sci U S A* **109**, 8346-8351 (2012).
70. Hart, Y.*, et al.* Paradoxical Signaling by a Secreted Molecule Leads to Homeostasis of Cell Levels. *Cell* **158**, 1022-1032 (2014).
71. Korem Kohanim, Y., Tendler, A., Mayo, A., Friedman, N. & Alon, U. Endocrine Autoimmune Disease as a Fragility of Immune Surveillance against Hypersecreting Mutants. *Immunity* **52**, 872-884.e875 (2020).
72. Sassone-Corsi, P. The Cyclic AMP Pathway. *Cold Spring Harbor Perspectives in Biology* **4**(2012).
73. Gallione, C.J. & Rose, J.K. A single amino acid substitution in a hydrophobic domain causes temperature-sensitive cell-surface transport of a mutant viral glycoprotein. *Journal of virology* **54**, 374-382 (1985).
74. Rahman-Zaman, A., Shan, S. & Reinhart-King, C.A. Cell migration in microfabricated 3D collagen microtracks is mediated through the prometastatic protein girdin. *Cellular and molecular bioengineering* **11**, 1-10 (2018).
75. Lopez-Sanchez, I.*, et al.* GIV/Girdin is a central hub for profibrogenic signalling networks during liver fibrosis. *Nature communications* **5**, 1-18 (2014).
76. Prieto-Dominguez, N., Parnell, C. & Teng, Y. Drugging the Small GTPase Pathways in Cancer Treatment: Promises and Challenges. *Cells* **8**(2019).

77. Kiyatkin, A., van Rosenburgh, I.K.v.A., Klein, D.E. & Lemmon, M.A. Kinetics of receptor tyrosine kinase activation define ERK signaling dynamics. *Science Signaling* **13**(2020).
78. Fritz, R.D.*, et al.* A versatile toolkit to produce sensitive FRET biosensors to visualize signaling in time and space. *Science signaling* **6**, rs12-rs12 (2013).
79. Midde, K.K.*, et al.* Multimodular biosensors reveal a novel platform for activation of G proteins by growth factor receptors. *Proceedings of the National Academy of Sciences* **112**, E937-E946 (2015).
80. Andrews, S.S., Peria, W.J., Richard, C.Y., Colman-Lerner, A. & Brent, R. Push-pull and feedback mechanisms can align signaling system outputs with inputs. *Cell systems* **3**, 444-455. e442 (2016).
81. Andrews, S.S., Brent, R. & Balázsi, G. Signaling Systems: Transferring information without distortion. *Elife* **7**, e41894 (2018).
82. Stolerman, L.M., Ghosh, P. & Rangamani, P. Stability analysis of a signaling circuit with dual species of GTPase switches. *arXiv preprint arXiv:2009.08356* (2020).
83. Arvan, P., Zhao, X., Ramos‐Castaneda, J. & Chang, A. Secretory pathway quality control operating in Golgi, plasmalemmal, and endosomal systems. *Traffic* **3**, 771-780 (2002).
84. Feizi, A., Gatto, F., Uhlen, M. & Nielsen, J. Human protein secretory pathway genes are expressed in a tissue-specific pattern to match processing demands of the secretome. *NPJ systems biology and applications* **3**, 1-9 (2017).
85. Austin, C.D. & Shields, D. Formation of nascent secretory vesicles from the trans-Golgi network of endocrine cells is inhibited by tyrosine kinase and phosphatase inhibitors. *The Journal of cell biology* **135**, 1471-1483 (1996).
86. Novick, P., Ferro, S. & Schekman, R. Order of events in the yeast secretory pathway. *Cell* **25**, 461-469 (1981).
87. Novick, P., Field, C. & Schekman, R. Identification of 23 complementation groups required for post-translational events in the yeast secretory pathway. *Cell* **21**, 205-215 (1980).
88. Schekman, R. & Orci, L. Coat proteins and vesicle budding. *Science* **271**, 1526-1533 (1996).
89. Hanahan, D. & Weinberg, R.A. Hallmarks of cancer: the next generation. *Cell* **144**, 646-674 (2011).
90. Doğaner, B.A., Yan, L.K.Q. & Youk, H. Autocrine Signaling and Quorum Sensing: Extreme Ends of a Common Spectrum. *Trends in cell biology* **26**, 262-271 (2016).
91. Kamino, K.*, et al.* Fold-change detection and scale invariance of cell-cell signaling in social amoeba. *Proc Natl Acad Sci U S A* **114**, E4149-e4157 (2017).
92. Tang, Y.*, et al.* An Autocrine Negative Feedback Loop Inhibits Dictyostelium discoideum Proliferation through Pathways Including IP3/Ca2+. *mBio* **12**, e01347-01321 (2021).
93. Tabassum, D.P. & Polyak, K. Tumorigenesis: it takes a village. *Nat Rev Cancer* **15**, 473-483 (2015).
94. Basanta, D. & Anderson, A.R.A. Exploiting ecological principles to better understand cancer progression and treatment. *Interface Focus* **3**(2013).
95. Li, X. & Thirumalai, D. Share, but unequally: a plausible mechanism for emergence and maintenance of intratumour heterogeneity. *Journal of The Royal Society Interface* **16**(2019).
96. Merlo, L.M.F., Pepper, J.W., Reid, B.J. & Maley, C.C. Cancer as an evolutionary and ecological process. *Nature Reviews Cancer* **6**, 924-935 (2006).
97. Basanta, D. & Anderson, A.R.A. Homeostasis Back and Forth: An Ecoevolutionary Perspective of Cancer. *Cold Spring Harbor Perspectives in Medicine* **7**(2017).
98. Maley, C.C.*, et al.* Classifying the evolutionary and ecological features of neoplasms. *Nature Reviews Cancer* **17**, 605-619 (2017).
99. Nechipurenko, I.V.*, et al.* A Conserved Role for Girdin in Basal Body Positioning and Ciliogenesis. *Dev Cell* **38**, 493-506 (2016).
100. Ha, A., Polyanovsky, A. & Avidor-Reiss, T. Drosophila Hook-Related Protein (Girdin) Is Essential for Sensory Dendrite Formation. *Genetics* **200**, 1149-1159 (2015).
101. Houssin, E., Tepass, U. & Laprise, P. Girdin-mediated interactions between cadherin and the actin cytoskeleton are required for epithelial morphogenesis in Drosophila. *Development* **142**, 1777-1784 (2015).
102. Puseenam, A.*, et al.* A novel Drosophila Girdin-like protein is involved in Akt pathway control of cell size. *Exp Cell Res* **315**, 3370-3380 (2009).
103. Yamaguchi, M., Suyari, O., Nagai, R. & Takahashi, M. dGirdin a new player of Akt /PKB signaling in Drosophila Melanogaster. *Front Biosci (Landmark Ed)* **15**, 1164-1171 (2010).

104. DiGiacomo, V., Marivin, A. & Garcia-Marcos, M. When Heterotrimeric G Proteins Are Not Activated by G Protein-Coupled Receptors: Structural Insights and Evolutionary Conservation. *Biochemistry* **57**, 255-257 (2018).
105. Milo, R.*, et al.* Network motifs: simple building blocks of complex networks. *Science* **298**, 824-827 (2002).
106. Shen-Orr, S.S., Milo, R., Mangan, S. & Alon, U. Network motifs in the transcriptional regulation network of Escherichia coli. *Nat Genet* **31**, 64-68 (2002).
107. Lo, I.C.*, et al.* Activation of Gαi at the Golgi by GIV/Girdin imposes finiteness in Arf1 signaling. *Dev Cell* **33**, 189-203 (2015).
108. Lane, J.R.*, et al.* Antibodies that identify only the active conformation of Gi family G protein α subunits. *The FASEB Journal* **22**, 1924-1932 (2008).
109. Marshansky, V., Bourgoin, S., Londono, I., Bendayan, M. & Vinay, P. Identification of ADP-ribosylation factor-6 in brush-border membrane and early endosomes of human kidney proximal tubules. *Electrophoresis* **18**, 538-547 (1997).
110. Velasco, A.*, et al.* Cell type-dependent variations in the subcellular distribution of alpha-mannosidase I and II. *J Cell Biol* **122**, 39-51 (1993).
111. Lopez-Sanchez, I.*, et al.* Focal adhesions are foci for tyrosine-based signal transduction via GIV/Girdin and G proteins. *Molecular biology of the cell* **26**, 4313-4324 (2015).
112. Rohena, C.*, et al.* GIV/Girdin and Exo70 Collaboratively Regulate the Mammalian Polarized Exocytic Machinery. *Iscience* **23**, 101246 (2020).
113. Ma, G.S.*, et al.* Therapeutic effects of cell-permeant peptides that activate G proteins downstream of growth factors. *Proceedings of the National Academy of Sciences* **112**, E2602-E2610 (2015).
114. Gibson, S.K. & Gilman, A.G. Gialpha and Gbeta subunits both define selectivity of G protein activation by alpha2-adrenergic receptors. *Proc Natl Acad Sci U S A* **103**, 212-217 (2006).
115. Bunemann, M., Frank, M. & Lohse, M.J. Gi protein activation in intact cells involves subunit rearrangement rather than dissociation. *Proc Natl Acad Sci U S A* **100**, 16077-16082 (2003).
116. Kean, M.J.*, et al.* VAMP3, syntaxin-13 and SNAP23 are involved in secretion of matrix metalloproteinases, degradation of the extracellular matrix and cell invasion. *Journal of cell science* **122**, 4089-4098 (2009).
117. Chung, H.J., Steplewski, A., Uitto, J. & Fertala, A. Fluorescent protein markers to tag collagenous proteins: The paradigm of procollagen VII. *Biochemical and biophysical research communications* **390**, 662-666 (2009).
118. Dell'Angelica, E.C.*, et al.* GGAsa family of ADP ribosylation factor-binding proteins related to adaptors and associated with the Golgi complex. *The Journal of cell biology* **149**, 81-94 (2000).
119. Adler, M.*, et al.* Endocytosis as a stabilizing mechanism for tissue homeostasis. *Proceedings of the National Academy of Sciences* **115**, E1926 (2018).
120. Kloeden, P.E. & Platen, E. Strong Taylor Approximations. in *Numerical Solution of Stochastic Differential Equations* (eds. Kloeden, P.E. & Platen, E.) 339-371 (Springer Berlin Heidelberg, Berlin, Heidelberg, 1992).
121. Franceschini, A.*, et al.* STRING v9.1: protein-protein interaction networks, with increased coverage and integration. *Nucleic Acids Research* **41**, D808-D815 (2013).
122. Sinha, S., Samaddar, S., Das Gupta, S.K. & Roy, S. Network approach to mutagenesis sheds insight on phage resistance in mycobacteria. *Bioinformatics* **37**, 213-220 (2021).
123. Ear, J.*, et al.* A long isoform of GIV/Girdin contains a PDZ-binding module that regulates localization and G-protein binding. *Journal of Biological Chemistry* **296**(2021).
124. Ghosh, P.*, et al.* Biochemical, biophysical and cellular techniques to study the guanine nucleotide exchange factor, GIV/Girdin. *Current protocols in chemical biology* **8**, 265-298 (2016).
125. Cohen, L.A. & Donaldson, J.G. Analysis of Arf GTP-binding protein function in cells. *Curr Protoc Cell Biol* **Chapter 3**, Unit 14 12 11-17 (2010).
126. Ghosh, P.*, et al.* A G{alpha}i-GIV molecular complex binds epidermal growth factor receptor and determines whether cells migrate or proliferate. *Mol Biol Cell* **21**, 2338-2354 (2010).
127. Manders, E., Stap, J., Brakenhoff, G., Van Driel, R. & Aten, J. Dynamics of three-dimensional replication patterns during the S-phase, analysed by double labelling of DNA and confocal microscopy. *Journal of cell science* **103**, 857-862 (1992).

128. Midde, K.K., *et al.* Multimodular biosensors reveal a novel platform for activation of G proteins by growth factor receptors. *Proc Natl Acad Sci U S A* **112**, E937-946 (2015).
129. Borejdo, J., Rich, R. & Midde, K. Mesoscopic analysis of motion and conformation of cross-bridges. *Biophys Rev* **4**, 299-311 (2012).
130. Broussard, J.A., Rappaz, B., Webb, D.J. & Brown, C.M. Fluorescence resonance energy transfer microscopy as demonstrated by measuring the activation of the serine/threonine kinase Akt. *Nature protocols* **8**, 265 (2013).
131. Roszik, J., Lisboa, D., Szöllősi, J. & Vereb, G. Evaluation of intensity‐based ratiometric FRET in image cytometry—Approaches and a software solution. *Cytometry Part A* **75**, 761-767 (2009).
132. Midde, K., *et al.* Membrane topology of human presenilin-1 in SK-N-SH cells determined by fluorescence correlation spectroscopy and fluorescent energy transfer. *Cell biochemistry and biophysics* **70**, 923-932 (2014).
133. Midde, K., *et al.* Comparison of orientation and rotational motion of skeletal muscle cross-bridges containing phosphorylated and dephosphorylated myosin regulatory light chain. *J Biol Chem* **288**, 7012-7023 (2013).
134. Presley, J.F., *et al.* ER-to-Golgi transport visualized in living cells. *Nature* **389**, 81-85 (1997).

AUTHOR CONTRIBUTIONS

L.Q carried out and analyzed all modeling studies in this work. A.A.A., I-C.L, and C.R designed, carried out and analyzed most of the experiments and assembled the figures. T.N extracted the Golgi-specific proteome from the human cell map and performed the GO analyses; SS performed the protein-protein network analyses. V.G. performed VSVG transport assays; N.A and I-C.L performed the MMP and collagen secretion assays. K.M. and I.L-S carried out and analyzed the FRET and Gαi:GTP assays, respectively. L.Q, AAA, I-C.L and V.G. helped write methods and edit the manuscript. P.G. and M.G.F conceptualized, designed, supervised and analyzed the experiments. P.R, with input from P.G, conceptualized, designed, supervised and analyzed the modeling studies. P.G and P.R wrote the manuscript.

ACKNOWLEDGEMENTS

We thank Linda Joosen for technical assistance with FRET assays. This work was supported by the National Institute of Health Grants: CA238042, AI141630 and CA160911 (to P.G.), GM132106 (to P.R), CA100768 (to M.G.F and P.G). P.R was also supported by the Air Force Office of Scientific Research (AFOSR) Multidisciplinary University Research Initiative (MURI) Grant FA9550-18-1-0051. I-C. L. was supported in part by a Fellowship (NSC 100-2917-1-564-032) from the National Science Council of Taiwan, K.M. by Susan G. Komen award (# PDF14298952) and I.L-S by the American Heart Association (AHA #14POST20050025). A.A.A was supported, in part, by an NIH-funded Cancer Therapeutics Training Program (CT2, T32 CA121938).

DECLARATION OF INTERESTS

The authors declare no competing interests.

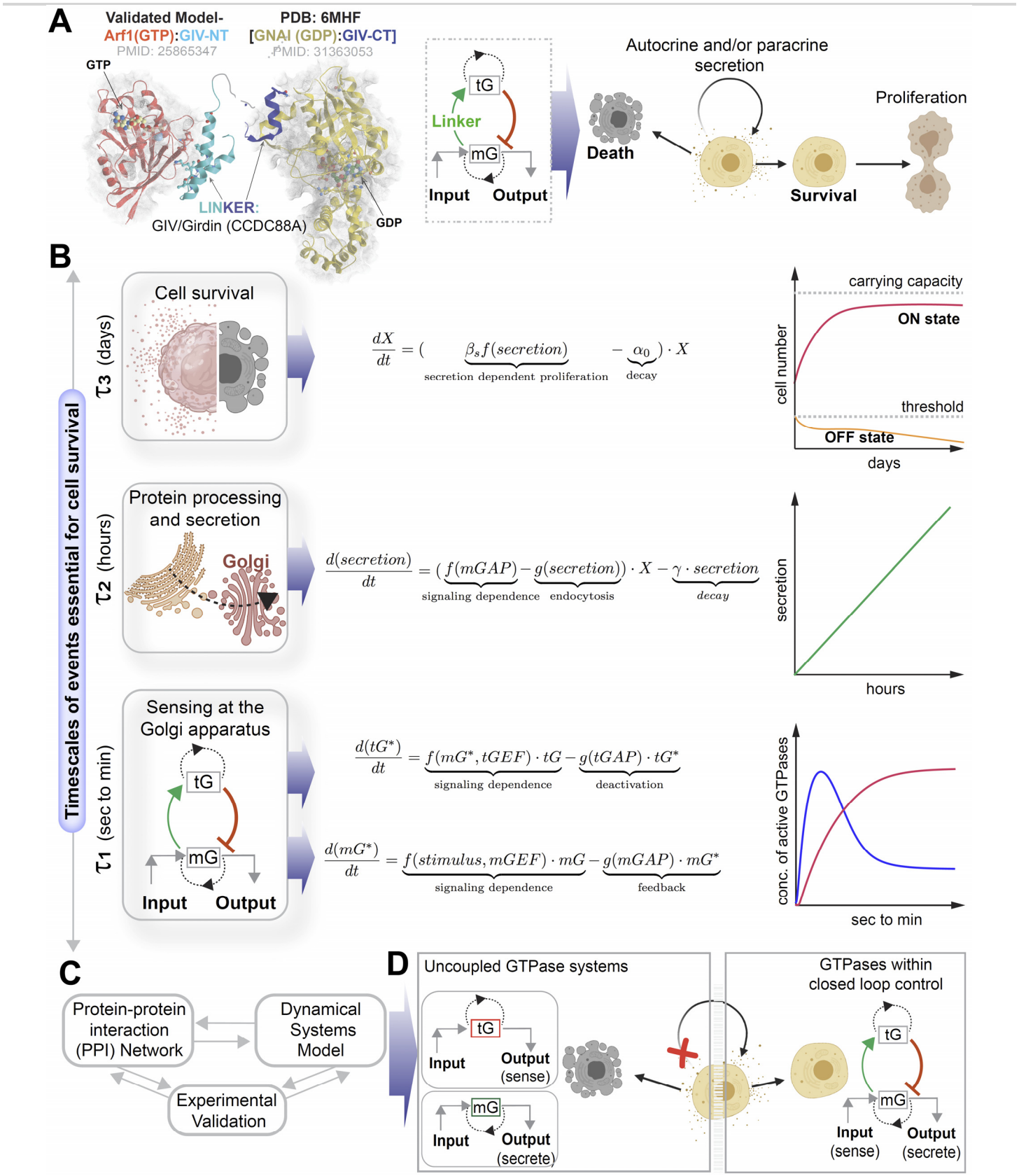

Figure 1. Study design, approach, and summary of findings.

A. Schematic shows a system of two species of GTPases, mGTPases (mG) and heterotrimeric GTPases (tG), coupled by a linker protein, GIV/Girdin, that is localized on the Golgi membranes within the secretory pathway as the focus of this study. The circuit begins when active Arf1-GTP directly binds GIV's N-term HOOK domain, recruits GIV to Golgi membranes, and activates Gi[107] (single forward loop, green). The circuit is completed when GIV's C-terminus orchestrates two feedback loops (red), both of which are essential for the inactivation of Arf1[107]: While the existence of such coupling[18] and its structural basis has been demonstrated before[18,24], the role of such coupling in autocrine secretion-supported cell survival and proliferation is studied here.

B. The dynamical systems model to describe the events presented in **A** is shown. This model is based on the nominal time scale of these events (left panel) and has the typical behavior shown in the right panel.

C. Overview of cross-disciplinary approaches used in this work to dissect the role of the coupled GTPases within the secretory pathway, generate testable hypotheses, and test them experimentally.

D. Schematic showing the final conclusions drawn from the study. Coupling of the two GTPases was found to be necessary for connecting sensing to secretion, and subsequently to cell survival. Uncoupling the GTPases or interrupting autocrine secretion (red cross) triggers cell death.

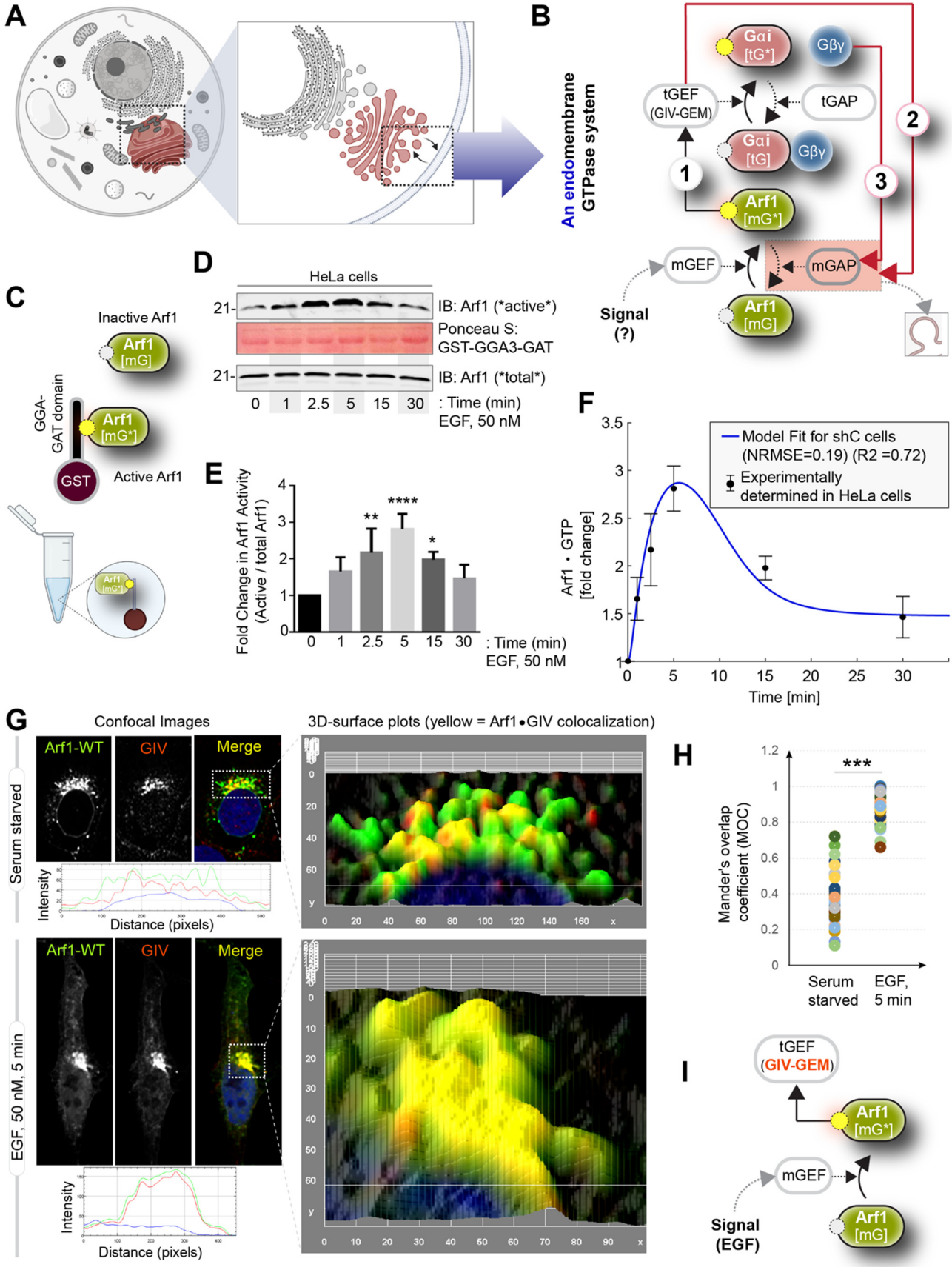

Figure 2. EGF activates Arf1 (mG*) within the Golgi-localized endomembrane GTPase system, triggers the recruitment of GIV-GEM on Golgi.

A. Schematic showing a Golgi-localized endomembrane GTPase system comprised of two distinct species of GTPases, monomeric (m) and trimeric (t), which regulates Golgi processes.

B. Components of that system are shown on left. Arrows denote key molecular events/chemical reaction cascades within this system, in which, the GIV-GEM links monomeric (m) and trimeric (t) GTPase systems and enable the conversion of extracellular stimuli (ligand; left) into membrane trafficking events (e.g., vesicle uncoating/budding/fusion; right). See also **Supplementary Figure S1** for illustrations detailing the sequential steps within the dynamic nature of the motif, and **Supplemental Information (Movie 1)** for the visualization of these dynamic steps as a movie gif.

C. Schematic outlines the biochemical approach to studying the proportion of Arf activation in cells using GST-GGA-GAT domain. Bound fraction represents active and unbound fraction represents inactive conformation.

D. Immunoblot shows bound Arf1 (active; top) and total Arf1 (input lysates; bottom) from equal aliquots of lysates of HeLa cells that were stimulated with EGF for the indicated time points prior to lysis.

E. Bar graphs display the fold change in Arf1 activity normalized to t0 min. Results are expressed as mean ± S.E.M; n = 3 replicates; *p* values were determined using Mann-Whitney t-test compared to t0: *, <0.05; **, <0.01; ***, <0.001. Immunoblots are representative of findings from at least 3 independent repeats.

F. Graph displays an overlay of experimentally determined Arf1 activation dynamics (results are displayed as mean ± S.E.M; n=3) and simulations (blue continuous line) in control cells where m and t-GTPases are coupled.

G. HeLa cells expressing Arf1-HA were serum starved overnight (G, top) and subsequently stimulated with EGF for 5 min (G, bottom) prior to fixation with PFA. Fixed cells were stained for Arf1 (HA; green) and GIV (red) and nuclei (DAPI; blue). Panels on the left show overlay of all 3 stains and representative RGB plots of sections through the Arf1-stained pixels. Panels on the right display the magnified 3D surface plots of the boxed regions in the left panels.

H. Scatter plot shows the Mandler's overlap coefficient (MOC) for Arf1-HA and GIV colocalization in G that was calculated on 13-15 cells/experiment, n = 3 independent experiments. *p* values were determined using Mann-Whitney t-test: ***, <0.001.

I. Schematic summarizing the experimentally determined steps within the Golgi-localized endomembrane GTPase system that are triggered by EGF.

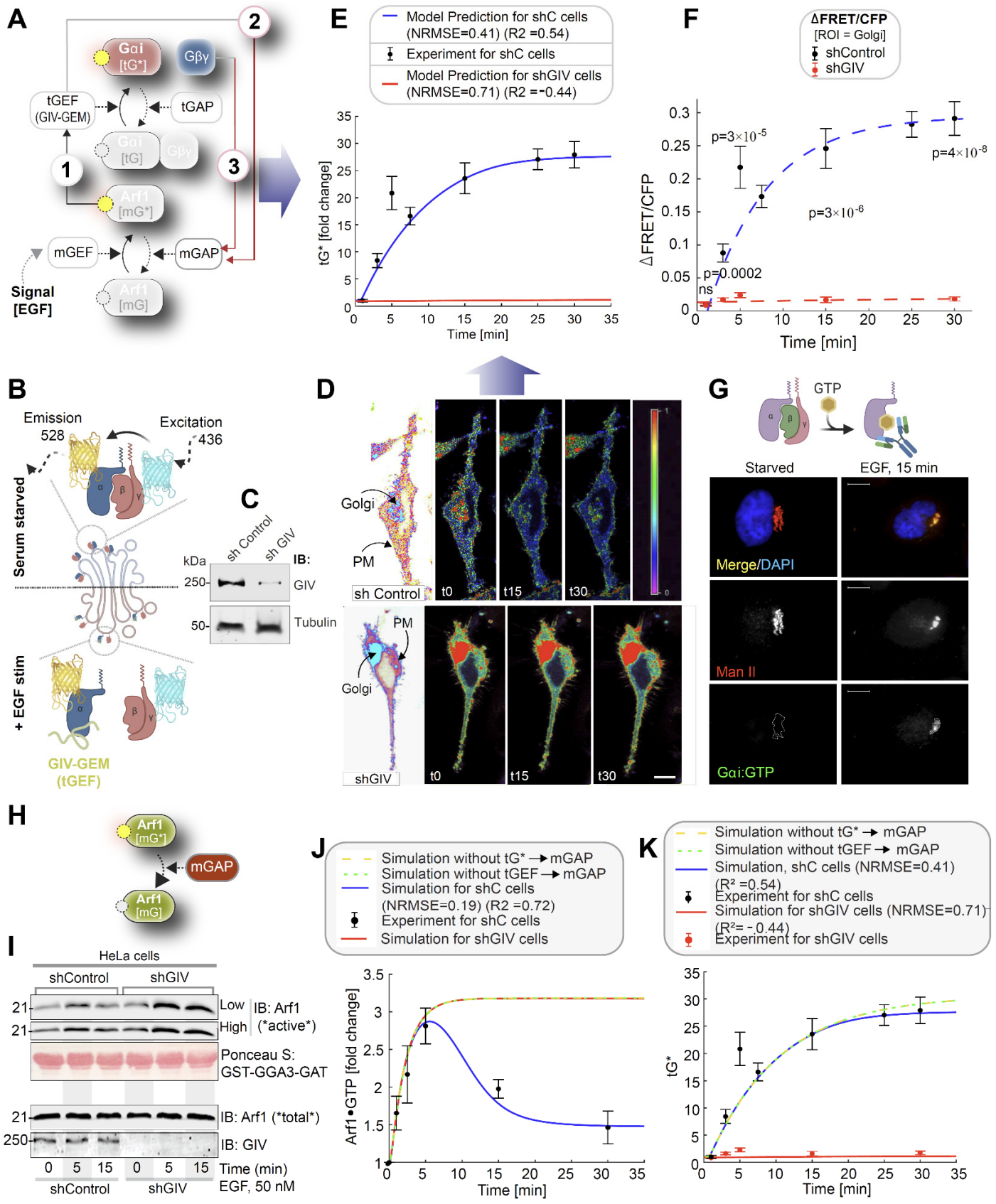

Figure 3. EGF triggers activation of Gi (tG*) on Golgi membranes and terminates Arf1 signaling, requires GIV-GEM.

A. Schematic showing the specific step within the endomembrane GTPase system being interrogated in this figure.

B. Schematic describing the mechanism of the FRET Gαi activity reporter. Serum starved conditions are expected to have more inactive trimeric Gi, and hence show high FRET (top). Upon ligand stimulation GIV-dependent dissociation of trimers is expected, with a resultant loss of intermolecular FRET.

C. Equal aliquots (~45 µg) of whole cell lysates of control (sh Control; top) and GIV-GEM depleted (shGIV; bottom) HeLa cells were analyzed for GIV and tubulin (loading control) by immunoblotting (IB).

D. Control (sh Control; top) and GIV-GEM depleted (shGIV; bottom) HeLa cells were co-transfected with Gαi1-YFP, Gβ1-CFP and Gγ2 (untagged) and live cells were analyzed by FRET imaging at steady-state, after being serum starved in 0.2% FBS overnight and then after stimulation with 50 nM EGF. Representative freeze-frame FRET images are shown. FRET image panels display intensities of acceptor emission due to efficient energy transfer in each pixel. FRET scale is shown in inset. Golgi and PM regions of interest are indicated with arrows. Scale bar = 10 µm. See also **Figure S2A** for free-frame images for additional time points in control HeLa cells.

E-F. Continuous line graphs in E displays the results from the simulation of the EGF-triggered kinetics of tG* activation at the Golgi in shControl (blue) and shGIV cells (red). Overlayed experimentally derived data (derived from D) is represented as error bars (± S.E.M). Interrupted line graphs in F display the quantification of FRET results from during a 30 min period after EGF stimulation. Results are expressed as mean ± S.E.M. Data represent 5 regions of interest (ROIs) analyzed over the pixels corresponding to the Golgi of 3-5 cells from 2 independent experiments. *p* values, as determined against t0 using Mann-Whitney are displayed.

G. *Top*: Schematic showing how a conformation-specific anti-Gαi•GTP antibody detects GTP-bound active Gαi in situ. *Bottom*: HeLa cells starved with 0.2% FBS overnight or stimulated subsequently with 50 nM EGF were fixed and stained for active Gαi (green; anti-Gαi:GTP mAb) and Man II (red) and analyzed by confocal microscopy. Activation of Gαi was detected exclusively after EGF stimulation. When detected, active Gαi colocalizes with Man II (yellow pixels in merge panel). See also **Figure S2B** for additional time points and stimuli. Scale bar = 7.5 µm.

H. Schematic shows the step within the endomembrane GTPase system being interrogated in panels H-J.

I. Immunoblot in C shows bound Arf1 (active; top) and total Arf1 (input lysates; bottom) from equal aliquots of lysates of control (sh Control) and GIV-depleted (shGIV) HeLa cells that were stimulated with EGF for the indicated time points prior to lysis. Bar graphs in **Figure S3A** display the fold change in Arf1 activity normalized to t0 min.

J. Line graphs display the simulations of Arf1 activation dynamics (mG*) in cells without tGEF (shGIV; red), or for other conditions in which one or the other negative feedback loops are missing (interrupted yellow and green continuous line graphs). As a reference, results of the simulation fit to experimental data in control cells are displayed in blue.

K. Line graphs display the simulations of Gαi (tG*) activation dynamics in cells without tGEF (shGIV; red), or for other conditions in which one or the other negative feedback loops are missing (interrupted yellow and green continuous line graphs). As a reference, results of the simulation fit to experimental data in control cells are displayed in blue.

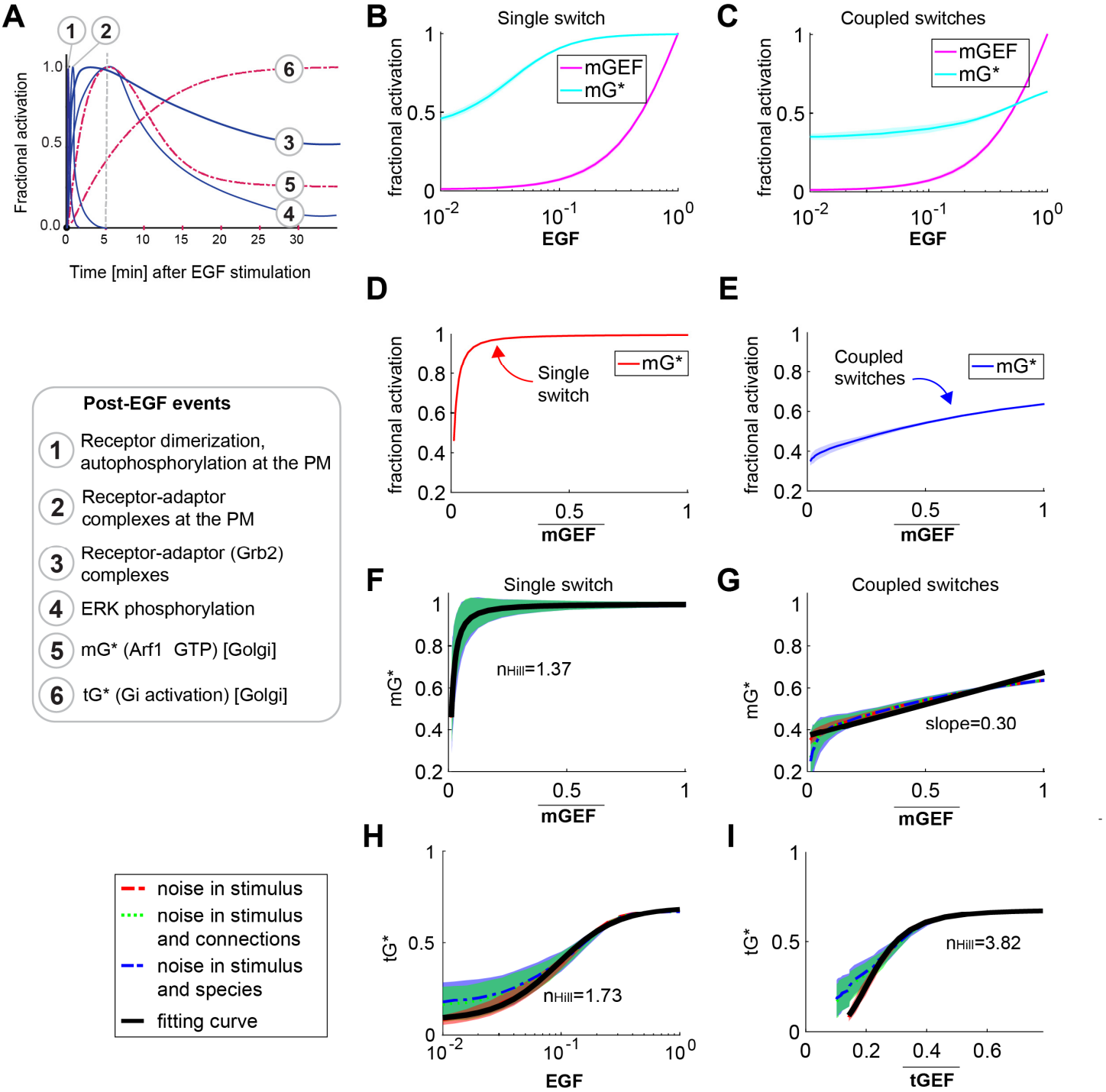

Figure 4. Coupled switches enable the alignment of endomembrane responses (Arf1 and tG* activities) to the dose of extracellular stimuli.

A. Published dynamics of EGF-stimulated events that are initiated at the PM (blue, continuous) or experimentally determined dynamics of events at the Golgi confirmed here (red, interrupted) are compared.

B-C. Dose responses of fractional activations of mGEF and active Arf1 (mG*) for the single switch (B; mG alone) and coupled switches (C; mG and tG). We perform stochastic simulations in the presence of noise in EGF (see STAR Methods for details). The mean and the standard deviation (SD) of species are evaluated at steady states.

The dimensionless EGF concentrations in the simulations are obtained through normalization, i.e., dividing the EGF concentration by 217.4 nM (=50 nM/0.23). In all simulations, noise is introduced only in stimuli (i.e., EGF).

D-E. Relationships between active Arf1 and mGEF for the single switch (D) and coupled switches (E). $\overline{mGEF}$ denotes the mean of mGEF. Data (derived from B-C) are shown as mean values, with the shading showing the SD. In all simulations, noise is introduced only in stimuli (i.e., EGF).

F-G. The same plots as in D-E but in the presence of three different types of noise: noise in stimulus (shown in red), noise in stimulus and connections simultaneously (shown in green), and noise in stimulus and species simultaneously (shown in blue) (see *STAR methods* for details). Data are shown as mean values (dashed curves), with the shading showing the SD. The black curves are fitting curves (r^2>0.95) for red dashed curves (See STAR Methods for the calculations of r^2 and n_{Hill}).

H-I. The fractional activations of tGTPase (tG*) as a function of EGF (H) or tGEF (I). The plots are generated in the similar way as in F-G. $\overline{tGEF}$ denotes the mean of tGEF. r^2>0.95 for all fitting curves.

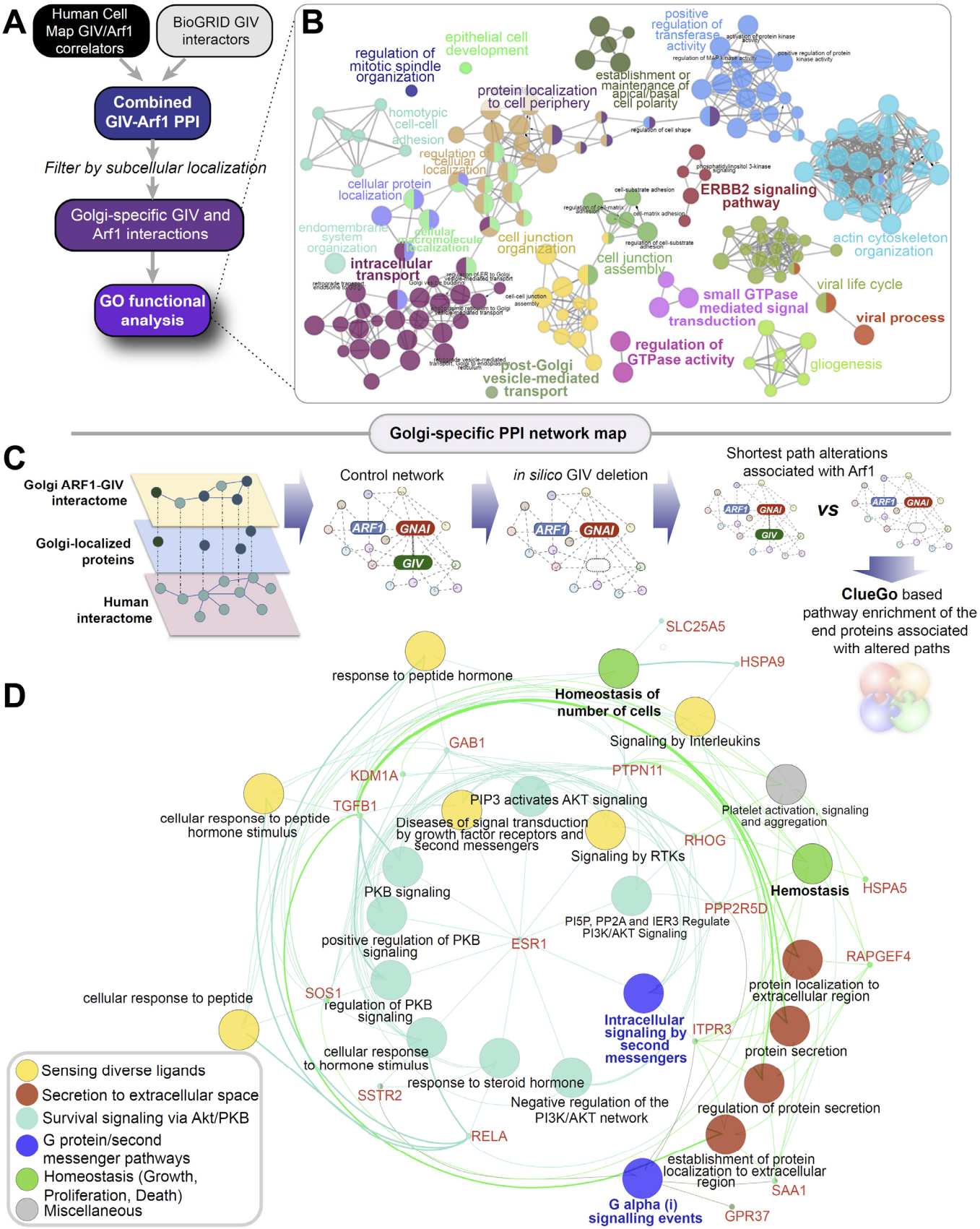

Figure 5. Prediction of cellular consequences of uncoupling the Golgi-localized GTPase circuitry by PPI network analyses.

A. Workflow for extracting the proteins that bind Arf1 and GIV and are localized at the Golgi. The complete list of these proteins is provided as **Supplemental Dataset 2**.

B. Gene Ontology (GO) analysis of a Golgi-specific GIV and Arf1 interaction network, as visualized using ClueGO. Groups/clusters were collapsed and only those nodes are displayed that have the highest logP value.

C. Workflow for how the list of proteins in A were used to create a Golgi localized PPI network from the STRING database to fetch the linking nodes to connect the seed proteins. The network was then perturbed by *in silico* deletion of GIV, followed by topological analysis of how such perturbation impacts the shortest paths associated with Arf1 to all other nodes in the network (see STAR methods).

D. A network representation using the ClueGo algorithm of the cellular processes associated with the end proteins that were most frequently encountered in the most impacted shortest paths associated with Arf1 (listed in **Figure S5E**). The deleted or newly added shortest paths were only considered using differential network approach. (see STAR methods) The key on the lower left corner displays the color code of various overarching themes encountered in the network.

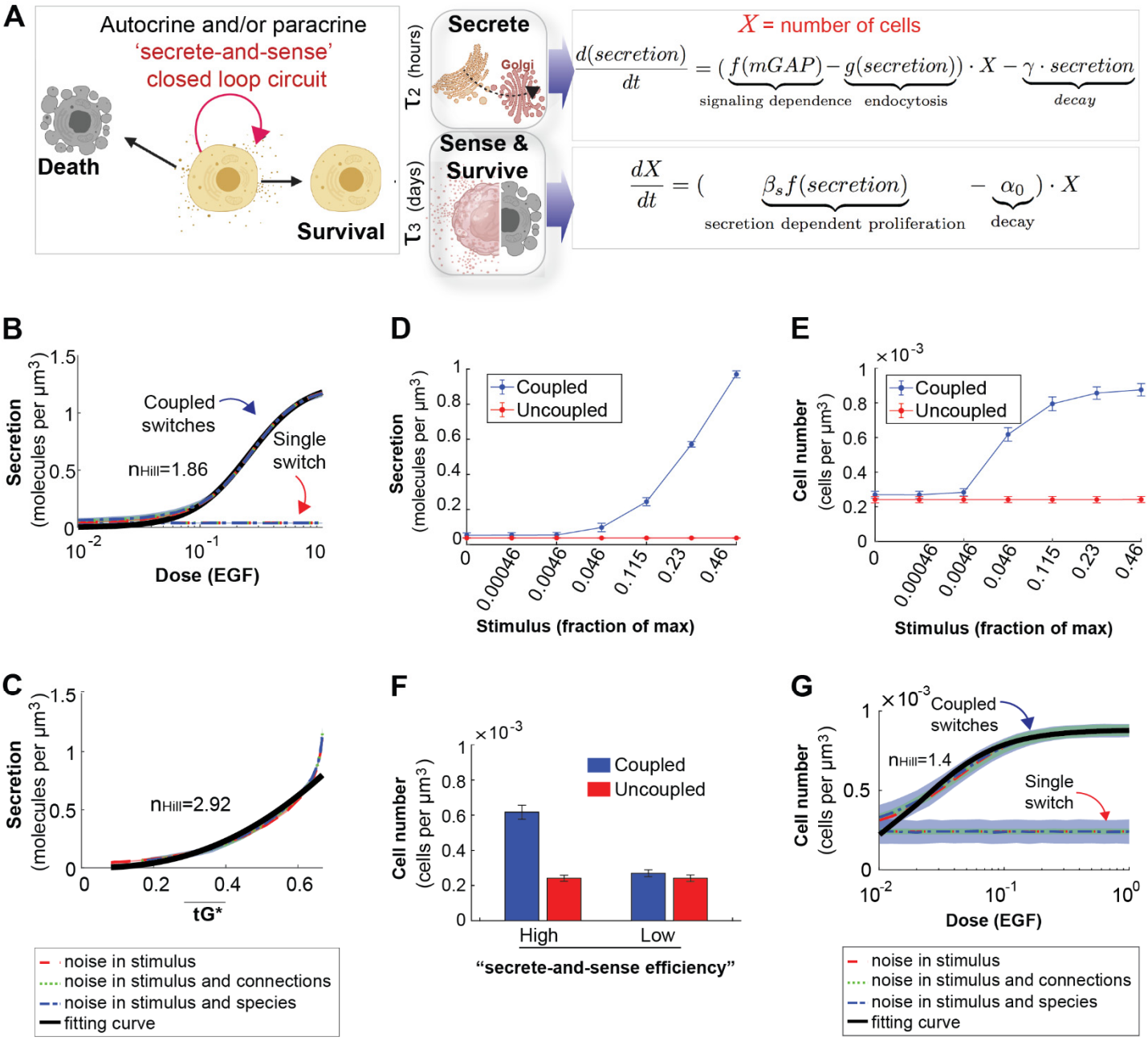

Figure 6. Coupled GTPases are predicted to support secrete-and-sense autonomy and for the maintenance of cell number.

A. Schematic of the key features of the auto/paracrine loop that we hypothesize is regulated by the coupled GTPase circuit (left) and the corresponding phenomenological models to capture these key effects (right).

B-C. Model prediction for secretion as a function of stimulus in cells with coupled and uncoupled GTPases. Noise is introduced into the system in a similar way as described in **Figure 4F-I**. r^2>0.99 in B; r^2>0.94 in C.

D-E. The secretion (D) or the cell number (E) as a function of stimulus in coupled and uncoupled switches. The stimulus =0, 0.00046, 0.0046, 0.046, 0.115, 0.23 and 0.46 correspond to varying doses of EGF in simulations, ranging

from 0, 0.1 nM, 1 nM, 10 nM, 25 nM, 50 nM, and 100 nM, respectively. The error bar denotes the S.D when noise is in the stimulus and connections.

F. The bar plot depicts cell numbers achieved by cells with either coupled or uncoupled switches, at different levels of stimulus. The first two bars represent the cell number when stimulus =0.046, and the last two bars are for stimulus =0. Noise is introduced as in B-C.

G. Relation between cell number and EGF in the presence of noise, which was introduced in a similar way as described in **Figure 4F-I**. r^2>0.95.

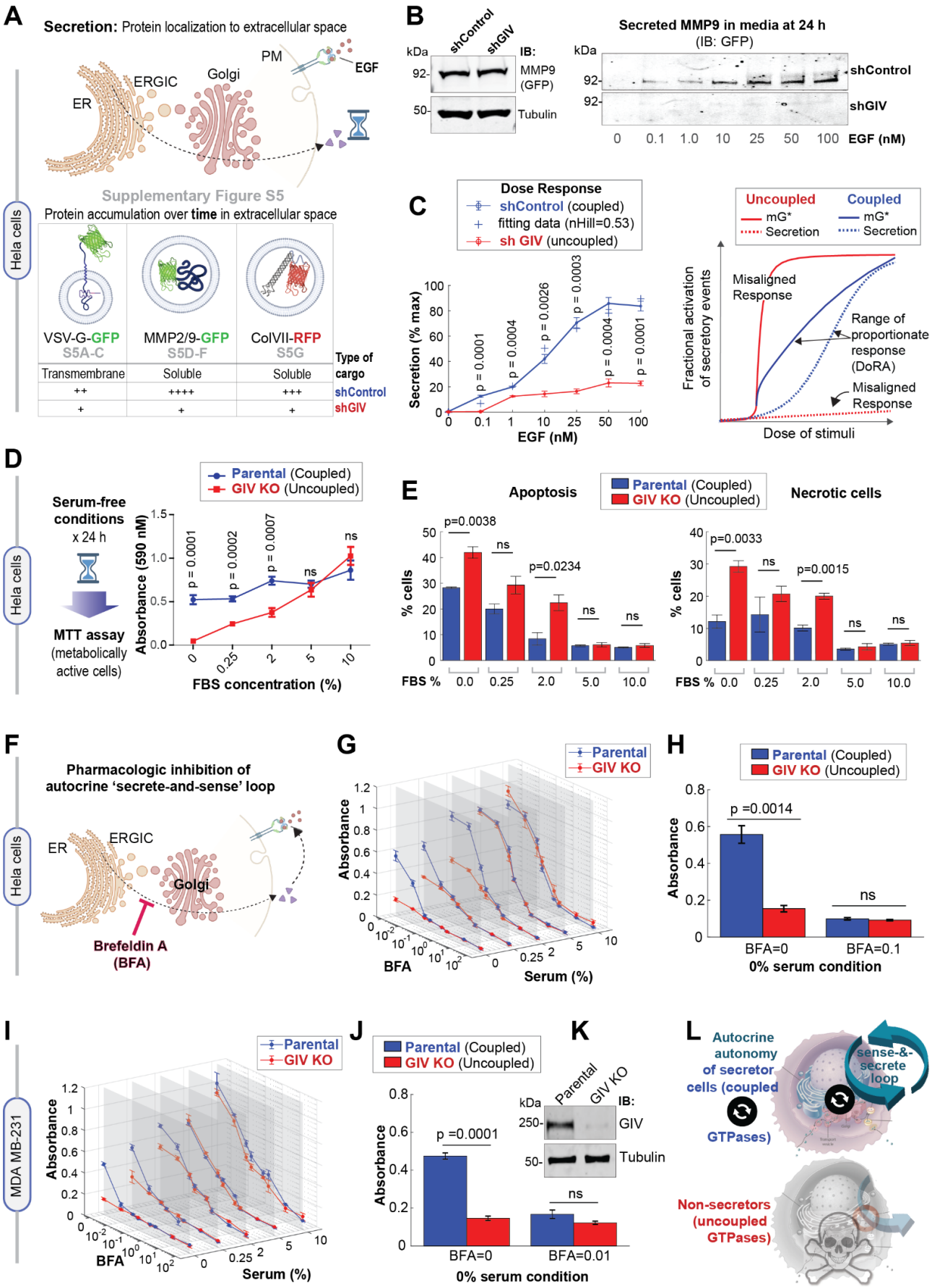

Figure 7. Coupling of GTPases by GIV is required for growth factor-independent cell survival that relies upon

autocrine secretion.

A. Schematic summarizes the findings showcased in **Supplementary Figure S5**, which investigate the secretion of diverse cargo proteins [temperature-sensitive (ts) VSV-G, MMP2/9 and ColVII], as determined by their accumulation in extracellular space over time after stimuli (EGF or serum). For each cargo tested, compared to cells with GIV (shControl), ligand-stimulated secretion was impaired in cells without GIV (shGIV).

B. Immunoblots showing intracellular (left) and secreted (in the media; right) GFP-MMP9 at 24 h after stimulation with varying doses of EGF. Tubulin, used as loading control, confirm the presence of a similar number of plated cells in the assay.

C. *Left*: Graph displays experimentally determined secretion of GFP-MMP9 in response to varying doses of EGF in control (shControl) and GIV-depleted (shGIV) HeLa cells (as in B), and quantified by band densitometry. Results are expressed as mean ± S.E.M; n = 3. p values were determined by unpaired t-test. *Right*: Schematic diagram of dose responses (mG* and secretion) for the single switch and coupled switches. Coupled switches stretch the range of proportionate responses. Single mG switch results in misaligned responses. DoRA, dose response alignment.

D. Left: Schematic summarizing the colorimetric assay used here to determine the number of metabolically viable cells. Right: The graph displays formazan absorbance expressed as a measure of cell viability from the HeLa cells (Y axis) cultured at varying conc. of serum (X axis). Results are expressed as mean ± S.E.M; n = 3. p values were determined by unpaired t-test.

E. Bar graphs display the % apoptotic (*left*) or necrotic (*right*) control (parental) and GIV-depleted (GIV KO) HeLa cells after 24 h growth in varying concentration of serum, as assessed by annexin V staining and flow cytometry. See also **Supplementary Figure S6A-C** for dot plots and early and late apoptotic fractions. Results are expressed as mean ± S.E.M; n = 3. p values were determined by unpaired t-test.

F. Schematic showing the rationale for and mechanism of action of fungal toxin, BFA, for interrupting the secrete-and-sense autocrine loop in cells.

G-H. Control (parental) and GIV-depleted (GIV KO) HeLa cells grown in different concentrations of serum (FBS%) were treated or not with varying concentrations of BFA (μM) as indicated. Line graphs in 3D (G) depict the formazan absorbance expressed as a measure of cell viability from the HeLa cells in various conditions tested. Bar graphs (H) depict the cell number in serum-free growth conditions that are supported exclusively by autocrine secrete-and-sense loop (without BFA; BFA = 0.0 μM) or when such loop is interrupted (BFA = 0.1 μM).

I-K. Control (parental) and GIV-depleted (GIV KO) MDA MB-231 cells grown in different concentrations of serum (FBS%) were treated or not with varying concentrations of BFA (μM) as in G-H. Line graphs in 3D (I) depict the formazan absorbance expressed as a measure of cell viability from the MDA MB-231 cells in various conditions tested. Bar graphs (J) depict the viability of the MDA MB-231 cells in serum-free growth conditions that are supported exclusively by autocrine secrete-and-sense loop (without BFA; BFA = 0.0 μM) or when such loop is interrupted (BFA = 0.1 μM). Immunoblots (K) of equal aliquots of whole cell lysates confirm the depletion of GIV compared to tubulin (loading control).

L. Schematic summarizing the conclusions of this work. *Top*: Coupling of GTPases within the secretory pathway enables dose-response alignment of secretion to stimuli, which appears to be essential for 'secrete-and-sense' autocrine autonomy in cancer cells. *Bottom*: Uncoupling of the GTPases within the secretory pathway disrupts such autonomy and leads to cell death.

KEY RESOURCES TABLE

REAGENT or RESOURCE	SOURCE	IDENTIFIER
Antibodies		
Mouse monoclonal anti- Gαi-GTP	*Graeme Milligan* [108]	26901
Rabbit anti-Arf1	*Paul Randazzo* [109]	n/a
Rabbit anti-Mannosidase (Man)-II	*Gift from K. Moreman* [110]	n/a
Anti-GFP	*Living Colors, Invitrogen (Thermo Scientific)*	Catalog # MA5-15256
Anti-RFP	*Invitrogen (Thermo Scientific)*	Catalog # MA5-15257
Anti-GIV coiled coil antibody	*Millipore (Sigma)*	ABT80
Goat anti-Rabbit IgG, Alexa Fluor 594 conjugated	ThermoFisher Scientific	A11072
Goat anti-Mouse IgG, Alexa Fluor 488 conjugated	ThermoFisher Scientific	A11017
IRDye 800CW Goat anti-Mouse IgG Secondary (1:10,000)	LI-COR Biosciences	926-32210
IRDye 680RD Goat anti-Rabbit IgG Secondary (1:10,000)	LI-COR Biosciences	926-68071
Biological samples		
n/a		
Chemicals, peptides, and recombinant proteins		
DAPI (4',6-Diamidino-2-Phenylindole, Dilactate)	Thermo Fisher Scientific	D3571
MTT	Millipore Sigma	475989-1GM
Puromycin	Sigma	P9620-10ML
Brefeldin A	Sigma	B6542-5MG
Fetal Bovine Serum	PEAK SERUM	PS-FB1
Paraformaldehyde 16%	Electron Microscopy Biosciences	15710
Glutathione Sepharose[â] 4B	Sigma-Aldrich	GE17-0756-04
Protease inhibitor cocktail	Roche	11 873 580 001
Tyr phosphatase inhibitor cocktail	Sigma-Aldrich	P5726
Ser/Thr phosphatase inhibitor cocktail	Sigma-Aldrich	P0044
PVDF Transfer Membrane, 0.45mM	Thermo Scientific	88518
Prolong Glass	Thermo Fisher Scientific	P36980
Paraformaldehyde 16%	Electron Microscopy Biosciences	15710
Guava Cell Cycle Reagent	Millipore Sigma	4700-0160
Commercial kits		
Dead Cell Apoptosis Kit with Annexin V Alexa Fluor™ 488 & Propidium Iodide (PI)	ThermoFisher Scientific	V13241
Experimental models: Cell lines		
HeLa parental	ATCC	ATCC® CCL-2
HeLa GIV KO (CRISPR Cas9)	*Prior work (https://www.biorxiv.org/content/10.1101/2021.07.21.452842v2)*	n/a
MDA-MB-231	ATCC	ATCC® HTB-26
MDA-MB-231 parental and GIV KO (CRISPR Cas9) lines	*Prior work (https://www.biorxiv.org/content/10.1101/2021.07.21.452842v2)*	n/a
HeLa shControl	*Prior work* [111] [112] [18]	n/a
HeLa shGIV	*Prior work*[112]	n/a
Cos7 shControl	*Prior work*[112] [113]	n/a
Cos7 shGIV	*Prior work*[112] [113]	n/a
COS7	ATCC	ATCC® CRL-1651™
HEK293T	ATCC	ATCC® CRL-1573™

Oligonucleotides		
n/a		
Recombinant DNA		
Internally tagged G□i_1-YFP	Moritz Bünemann [114,115] [79] [18]	N/A
Girdin CRISPR/Cas9 KO Plasmid (h2)	*Santa Cruz Biotechnology (SCBT) Inc.*	Sc-402236-KO-2
CFP-G□$_1$		
Temperature sensitive (ts)VSVG-eGFP	*Lo I et al.,* [18]	N/A
MMP2-GFP	Marc Coppolino [116]	N/A
MMP9-GFP	Marc Coppolino [116]	N/A
Col Vii-RFP	Anderzej Fertala [117]	N/A
GST GAT (GGA)	Stuart Kornfeld [118]	N/A
Other: Software		
ImageJ	National Institute of Health	https://imagej.net/Welcome
IX81 FV1000 inverted confocal laser scanning microscope	Olympus	n/a
ClueGO	Cytoscape	https://academic.oup.com/bioinformatics/article/25/8/1091/324247
NetworkX	Python	https://networkx.org
Gephi	Gephi	https://gephi.org
Prism	GraphPad	https://www.graphpad.com/scientific-software/prism/
LAS-X	Leica	www.leica-microsystems.com/products/microscope-software/p/leica-las-x-ls
Illustrator	Adobe	https://www.adobe.com/products/illustrator.html
Matlab	MathWorks	https://www.mathworks.com/
ImageStudio Lite	LI-COR	https://www.licor.com/bio/image-studio-lite/

1. Resource Availability

Contact for reagents, models, and computational tools

2. Experimental Model and Subject Details

1. Human Cell Lines (HeLa, Cos7, MDA MB-231)

3. Method Details

1. Modeling methods
   - Model Assumptions
   - Governing equations
   - Numerical Simulations for the deterministic model
   - Fitting against experimental data
   - Testing model
   - The stochastic model
   - Numerical Simulations for the stochastic model

2. Computational Methods
   - Protein-protein network creation, topological analysis and visualization

3. Experimental methods
   - Reagents and antibodies
   - Cell culture, transfection, ligand stimulation and lysis
   - Arf1 activation assays
   - Quantitative immunoblotting
   - Immunofluorescence and Confocal Microscopy
   - Image Processing
   - Förster Resonance Energy Transfer (FRET) studies
   - GFP-tsO45-VSVG transport assays
   - Metalloprotease and collagen secretion assays
   - MTT assays
   - Cell cycle and apoptosis analyses

4. Quantification and Statistical Analysis

1. Statistical Analysis
2. Replications

RESOURCE AVAILABILITY

Lead Contact

Further information and requests for resources and reagents should be directed to and will be fulfilled by the Lead Contact, Pradipta Ghosh (prghosh@ucsd.edu). All model-related queries could be alternatively directed to and will be fulfilled by Padmini Rangamani (prangamani@ucsd.edu).

Materials Availability:

- This study did not generate new unique reagents

Data and Code Availability:

Model for the dual GTPase motif can be accessed at https://github.com/RangamaniLabUCSD/Coupled-switches-secretion. The datasets and codes relevant to the protein-protein network analyses can be accessed at https://github.com/RangamaniLabUCSD/Coupled-switches-secretion. Software programs (listed in Key Resource Table) are all publicly accessible through valid licenses.

DETAILED METHODS:

Modeling approaches:

Model Assumptions: We restrict our modeling considerations to the secretory pathway on Golgi and its interactions with the cell survival. The secretory pathway on Golgi consists of mGTPases, tGTPases, their GEFs and GAPs, and the secretion machinery. In the secretory pathway on Golgi, EGF mediates the recruitment of GEF for mGTPase (mGEF) and triggers the activation of corresponding mGTPases. Then active mGTPase can recruit GIV to vesicles. GIV is GEF for tGTPase (tGEF), and subsequently activates tGTPase. Upon activation of tGTPase, $G\beta\gamma$ is released and activates the GAP for mGTPase (mGAP). Besides, mGAP is also regulated by GIV, which binds to mGAP and works as a co-factor for GAP activity. mGAP has a dual role in this circuit: one is to turn 'OFF' mGTPase, and the other is to promote the vesicle formation. The vesicle formation is essential for secretion, and the secreted growth factors lead to the cell proliferation. The increase of cell number in turn enhances the secretion.

To model the above circuit, we assume that

- The total number of each type of GTPases is a constant.
- The copy number of GAP for tGTPase (tGAP) is constant since it is not regulated by other species.
- The species are present in large enough quantities that deterministic approaches can be used to capture the dynamics of the system.
- The process of secretion can be modeled using a simplified function that depends on mGAP.

Therefore, the circuit is modeled by a set of ordinary differential equations with six species: active mGTPase, active tGTPase, mGEF, mGAP, tGEF, and the secreted growth factors. Besides, the cells survival number is also modeled by an ordinary differential equation. We note that our model does not include the spatial or mechanical aspects associated with these signaling pathways.

Governing equations: We model all the species interactions by normalized-Hill functions[27,28] to capture the overall input-output relationships. We did not consider all the intermediary steps in the signaling pathway for the sake of simplicity**.** When active tGTPase and tGEF both regulate mGAP, the "AND" logic is applied and modeled as $f_{act}(\mathrm{tGTPases}) \cdot f_{act}(\mathrm{tGEF})$. In addition, the proliferation of cells is regulated by secreted growth factors to ensure the homeostasis[70,119]. Thus, the dynamics of the system can be described by the following equations:

$$\frac{d[mGEF]}{dt}\tau_{mGEF} = \left(f_{act}^{(1)}(stimulus) + k_{mGEF}\right)Y_{mGEF} - [mGEF] \tag{1}$$

$$\frac{d[mGAP]}{dt}\tau_{mGAP} = \left(f_{act}^{(2)}([tGEF])f_{act}^{(3)}([tG^*]) + k_{mGAP}\right)Y_{mGAP} - [mGAP] \tag{2}$$

$$\frac{d[mG^*]}{dt}\tau_{mG^*} = \left(f_{act}^{(4)}([mGEF]) + k_{mG^*}\right)(1 - [mG^*]) - f_{act}^{(5)}([mGAP])[mG^*] \tag{3}$$

$$\frac{d[tGEF]}{dt}\tau_{tGEF} = \left(f_{act}^{(6)}([mG^*]) + k_{tGEF}\right)Y_{tGEF} - [tGEF] \tag{4}$$

$$\frac{d[tG^*]}{dt}\tau_{tG^*} = \left(f_{act}^{(7)}([tGEF]\,) + k_{tG^*}\right)(1 - [tG^*]) - f_{act}^{(8)}([tGAP])[tG^*] \tag{5}$$

$$\frac{dS}{dt} = \left(\beta_S\left(f_{act}^{(9)}([mGAP]) + k_S\right) - \alpha_S\frac{S}{S + K_2}\right)X - \gamma S \tag{6}$$

$$\frac{dX}{dt} = \left(\lambda\frac{S}{S + K_1}\left(1 - \frac{X}{K}\right) - \mu\right)X \tag{7}$$

where variables $[mGEF]$, $[mGAP]$, $[mG^*]$, $[tGEF]$,and $[tG^*]$ denote the fractional activation of mGEF, mGAP, mGTPase, tGEF, and tGTPase, respectively. Here, the fractional activation is the copy number divided by the maximal copy number, which changes between 0 and 1. The variable $stimulus$ denotes the input signal EGF; S is the concentration of secreted growth factors; X is the cell number. The τ's are time scales. For equations (1)-(6), k's are basal production rates, and Y's are maximal fractional activations for species. For the equation (6), β_S is the maximal secretion rate; α_S is the maximal endocytosis rate; γ is the degradation rate of secreted growth factors; K_2 is the binding affinity of secreted growth factors. For the equation (7), λ and μ are cell proliferation and death rates by the cells, respectively; K_1 is the value of S when the Hill function $\frac{S}{S+K_1}$ is 0.5; K is the carrying capacity: once the cell number is K, the cell proliferation rate is zero, preventing the cell number from exceeding K. The function $f_{act}^{(i)}$ $(\mathrm{i} = 1,2,\cdots,9)$ is the normalized-Hill function, which takes the following form:

$$f_{act}(X) = \begin{cases} \dfrac{BX^n}{K^n + X^n}, & if\ 0 \le X < 1 \\ 1, & if\ X \ge 1 \end{cases} \tag{8}$$

where $B = \frac{EC_{50}^n - 1}{2EC_{50}^n - 1}$ and $K = (B - 1)^{1/n}$. Here, EC_{50} and n are half-maximal activation and Hill coefficient respectively. With these choices of constants B and K, we have $f_{act}(0) = 0$, $f_{act}(EC_{50}) = 0.5$. It should be noted that constants B and K can be different in different functions $f_{act}^{(i)}$. In most cases, we used $k = 0$ and $Y \le 1$, so the maximal value of variables $(1 + k)Y$ is smaller than 1 to ensure the range of the fractional activation. But,

when we used a non-zero k, the variable may be larger than 1, and then we regard the variable as the relative activation, which is normalized by a number smaller than maximal copy number. We refer to this model as the coupled system throughout our study.

Single switch model

For the circuit that only contains the single switch of mGTPases, its dynamics is described by equations (1)-(3), except that the equation (2) is replaced by

$$\frac{d[mGAP]}{dt}\tau_{mGAP} = k_{mGAP}Y_{mGAP} - [mGAP] \tag{9}$$

Note that this equation also can be used to describe the dynamics of mGAP when the regulation from tGEF to mGAP or the regulation from active tGTPase to mGAP doesn't exist.

Numerical Simulations for the deterministic model: Numerical simulations were implemented in MATLAB. We use the solver ode15s to simulate the dynamics on the time interval [0,1440] minutes unless otherwise specified.

Fitting against experimental data: To fit the time course data for control cells and GIV-depleted cells, we manually tuned the parameters in our model until the normalized RMSE between simulated and measured fold changes of active Arf1 was less than 0.2 and that for active tGTPase less than 0.45. Moreover, parameters for the secretion and cell survival are taken from their biologically plausible ranges[119]. Our fitting goal was to capture the experimentally observed trends rather than obtain kinetic parameters since our model does not include all the reactions in the pathway(s). Here, the normalized RMSE is the RMSE over the mean value of all experimental data; the baseline for the simulation result is the initial fractional activation when simulating dynamics for control cells, and those for experimental Arf1 and tGTPase data are initial states in control cells. The obtained parameter values are listed in **Supplementary Table 1**. In all simulations, the initial condition is the starved state when $stimulus = 0$, and then $stimulus$ is set to be 0.23 to simulate the dynamics under the EGF-stimulated condition. In all simulations, we use normalized values of EGF concentrations. The normalization was conducted such that the value of 0.23 EGF used in simulations corresponds to 50 nM in the experiments. The dimensionless EGF concentrations in the simulations are obtained by dividing the EGF concentration by 217.4 nM (=50 nM/0.23).

Testing model: We verify that our setting in the model for GIV-deplete cells indeed makes the system behave like the uncoupled system. We set the maximal fractional activation of tGEF as 0.1 (i.e., $\mathrm{Y}_{tGEF} = 0.1$) but keep other parameters unchanged to model the system in GIV-depleted cells. The initial state is determined by the steady-state values of all species when the stimulus is zero, which are obtained as follows: we set *stimulus* zero and chose an arbitrary initial condition (e.g., all species are 0.5), and then simulated the deterministic dynamics on the time interval [0, 2400hr] to ensure that the steady state is reached. →Then we changed the stimulus to 0.23 to simulate the dynamics of all species when EGF=50 nM. We find that GIV-depleted cells more likely

behave as the uncoupled system (**FigS4A**). For these two systems, mGEF and mG* both increase upon the stimulus of EGF, and mGAP won't increase because of low activation of tGEF in GIV-depleted cells or the absence of the positive regulation from tGEF and tG* in the uncoupled system. Due to non-increasing level of mGAP, these two systems both show non-decreasing fractional activation of mG*, low secretion and low cell number. The only difference between these two systems is the dynamics of tGTPase switch: tGEF is low in GIV-depleted cells and thus cannot activate tG*, while in the uncoupled system the fractional activations of tGEF and tG* are both high. The schematics of these three systems are shown in **FigS4 B-D**.

The stochastic model: To investigate the impact of noise, we consider three different sources of noise: stimulus, species and connections. A noisy stimulus is modeled by the summation of the mean and a noise term $\eta_{sti}(t)$; another type of noise, originated from species, is generated by adding a noise term $\eta_{spe}(t)$ in the equation for each species, and $tGAP$ is also perturbed by a noise term $\eta_{spe}^{tGAP}(t)$; the third type of noise, which comes from connections, is modeled by adding a noise term $\eta_{link}(t)$ to each activation function f_{act} and nonlinear reaction rates in equations for the secretion and the cell number. Here, these noise terms are independent from each other and all modeled by the following Ornstein-Uhlenbeck process:

$$\tau_j^{noise} d\eta_j = -\eta_j dt + \sigma_j dW_t^j \tag{10}$$

where $j = sti, spe, link$, and W_t^j's are independently and identical distributed standard Wiener processes. This equation implies that $\eta_j(t)$ has zero mean and variance $\frac{\sigma_j^2}{2\tau_j^{noise}}$. The equations for active tGEF, the secretory protein and the cell number in the presence of noise are taken as an example: when noise exists only in species, the dynamics of active tGEF, the secretory protein and the cell number are described by

$$\frac{d[tGEF]}{dt}\tau_{mGEF} = \left(f_{act}^{(6)}([mG^*]) + k_{tGEF}\right)Y_{tGEF} - [tGEF] + \eta_{spe}^{tGEF} \tag{11}$$

$$\frac{dS}{dt} = \left(\beta_S\left(f_{act}^{(9)}([mGAP]) + k_S\right) - \alpha_S\frac{S}{S+K_2}\right)X - \gamma S + \eta_{spe}^{S} \tag{12}$$

$$\frac{dX}{dt} = \left(\lambda\frac{S}{S+K_1}\left(1-\frac{X}{K}\right) - \mu\right)X + \eta_{spe}^{X} \tag{13}$$

while the corresponding dynamics when noise are present in connections are governed by

$$\frac{d[tGEF]}{dt}\tau_{mGEF} = \left(f_{act}^{(6)}([mG^*]) + \eta_{link}^{tGEF} + k_{tGEF}\right)Y_{tGEF} - [tGEF] \tag{14}$$

$$\frac{dS}{dt} = \left(\beta_S\left(f_{act}^{(9)}([mGAP]) + k_S\right) + \eta_{link}^{S,1} - \alpha_S\frac{S}{S+K_2} + \eta_{link}^{S,2}\right)X - \gamma S \tag{15}$$

$$\frac{dX}{dt} = \left(\lambda\frac{S}{S+K_1}\left(1-\frac{X}{K}\right) + \eta_{link}^{X} - \mu\right)X \tag{16}$$

where η_{link}'s with different superscripts are independent noise terms.

Numerical Simulations for the stochastic model: Numerical simulations were implemented in MATLAB. We used the Milstein scheme[120] to numerically solve the noise term η_j ($j = sti, spe, link$), and used the Euler scheme to solve the dynamics of molecules on the time interval [0,1440min]. To be specific, the noise term η_j at $n+1$ time step is determined by the following manner ($\tau_j^{noise} = 1$):

$$\eta_j^{n+1} = \eta_j^n - \eta_j^n dt + \sigma_j \delta W_n + \frac{1}{2}\sigma_j^2[(\delta W_n)^2 - dt]$$

where dt is the time step, and δW_n obeys the normal distribution with mean zero and variance dt. Then, the activation of molecules or the cell number is solved by the Euler scheme. For example, when noise is only in stimulus, the mGEF at $n+1$ time step, denoted as $[mGEF]^{n+1}$, is obtained by the following equation:

$$[mGEF]^{n+1} = [mGEF]^n + dt\frac{1}{\tau_{mGEF}}\left(\left(f_{act}^{(1)}\left(stimulus + \eta_{sti}^{n+1}\right) + k_{mGEF}\right)Y_{mGEF} - [mGEF]^n\right),$$

the schemes to solve the equations (12) and (15) are

$$S^{n+1} = S^n + dt\left(\left(\beta_S\left(f_{act}^{(9)}([mGAP]^n) + k_S\right) - \alpha_S\frac{S^n}{S^n + K_2}\right)X - \gamma S^n + \left(\eta_{spe}^S\right)^{n+1}\right),$$

and

$$S^{n+1} = S^n + dt\left(\left(\beta_S\left(f_{act}^{(9)}([mGAP]^n) + k_S\right) + \left(\eta_{link}^{S,1}\right)^{n+1} - \alpha_S\frac{S^n}{S^n + K_2} + \left(\eta_{link}^{S,2}\right)^{n+1}\right)X - \gamma S^n\right),$$

respectively.

We compare coupled switches with the single switch of mGTPase for three different cases of noise: noise in the stimulus, noise in the stimulus and species simultaneously, and noise in the stimulus and connections simultaneously. The values of noise amplitudes used for simulations are listed as follows:

- When noise is only in the stimulus, the parameter σ_{sti} for $\eta_{sti}(t)$ is 0.02, and τ_{sti}^{noise} is 1.
- When noise is in the stimulus and species simultaneously, parameters σ_{sti} and τ_{sti}^{noise} for $\eta_{sti}(t)$ are the same as those when noise is only in stimulus. In addition, for the noise term $\eta_{spe}(t)$, $\tau_{spe}^{noise} = 1$, and σ_{spe} is 0.02 for all species except the secretion and cell number. Since the secretion and cell number have small reaction rates, σ_{spe}^S and σ_{spe}^X are set to be 2×10^{-5} and 2×10^{-6} respectively, and thus the noisy behaviors cannot overwhelm the deterministic behaviors.
- When noise is in the stimulus and connections simultaneously, parameters σ_{sti} and τ_{sti}^{noise} for $\eta_{sti}(t)$ are still the same as those when noise is only in stimulus. Moreover, $\tau_{link}^{noise} = 1$, and $\sigma_{link}^{noise} = 0.02$ for all species except that the cell number. The σ_{link}^X is 0.002 to ensure the same order of the noise and the production rate of cell number.

In this study, for a given input signal, we performed 1000 repeated simulations on the time interval [0 1440min] (with the steady state under this signal as the initial state). The time step dt is set to be 0.01.

Computational and bioinformatics approaches:

Identification of a Golgi-localized Arf1 and GIV interactome:

We have previously extracted an annotated subcellular localization network of high confidence GIV correlators (Ear et al, JBC), based on Human Cell Map (Go et al). Based on the same HCM data set, the set of high confidence Arf1 correlators were also extracted. Using the combined set of proteins that were correlated with GIV and Arf1, a full correlation network between each and every protein was extracted. Annotated unique GIV interactors from BioGRID (https://pubmed.ncbi.nlm.nih.gov/33070389/) were also incorporated to expand the GIV-Arf1 interaction network. To assign subcellular localization of the GIV interactors from BioGRID, they were first matched to subcellular localization as annotated by HCM. For those proteins that were not assigned by HCM, they were then matched to Gene Ontology (GO) Cellular Component terms, Uniprot (https://pubmed.ncbi.nlm.nih.gov/30395287/) and Human Protein Atlas (https://pubmed.ncbi.nlm.nih.gov/25613900/), which were all used as a guide to manually assign them based on their biological function. The complete list of this 'Golgi-localized Arf1-GIV interactome' is provided as **Supplementary Dataset 2**.

Protein-protein interaction network creation, topological analyses, and visualization:

The list of proteins (**Supplementary Dataset 2**) was used as 'seed' to generate the Golgi-specific Arf1-GIV network by fetching other connecting interactions and proteins from STRING database[121]. The shortest path NetworkX algorithm[122] was used to trace the connected proteins and interactions in between every possible pair of protein from the above-mentioned list. Highest possible interaction cutoff score was used to avoid false positive interactions. To check the effect of GIV deletion a similar network was prepared, except without GIV. Shortest path alteration fraction[122] associated with Arf1 was calculated using differential shortest path analysis of the original and GIV-depleted PPI network. Here only the paths having shortest path alteration fraction 1, were considered which indicated only the deleted or newly added shortest paths due to GIV deletion. GO Biological Process (BP) analysis of the proteins identified using shortest path alteration fraction analysis was performed using the Cytoscape tool ClueGO (https://academic.oup.com/bioinformatics/article/25/8/1091/324247) and significant GO BP terms were visualized.

***Experimental Model and Subject Details*:**

Cell lines and culture methods

HeLa, Cos7 and MDA-MB-231 cells were grown at 37°C in their suitable media, according to their supplier instructions, supplemented with 10% FBS, 100 U/ml penicillin, 100 µg/ml streptomycin, 1% L-glutamine, and 5% CO2.

GIV CRISPR/Cas9 Gene Editing and Validation:

Pooled guide RNA plasmids (commercially obtained from Santa Cruz Biotechnology; Cat# sc-402236-KO-2) were used to generate both HeLa and MDA MB-231 GIV KO lines as described before [123]. Briefly, these CRISPR/Cas9 KO plasmids consists of GFP and Girdin-specific 20 nt guide RNA sequences derived from the GeCKO (v2) library and target human Girdin exons 6 and 7. Plasmids were transfected into Hela and MDA-MB-231 cells using PEI. Cells were sorted into individual wells using a cell sorter based on GFP expression. To identify cell clones harboring mutations in gene coding sequence, genomic DNA was extracted using 50 mM NaOH and boiling at 95°C for 60mins. After extraction, pH was neutralized by the addition of 10% volume 1.0 M Tris-pH 8.0. The crude genomic extract was then used in PCR reactions with primers flanking the targeted site. Amplicons were analyzed for insertions/deletions (indels) using a TBE-PAGE gel. Indel sequence was determined by cloning amplicons into a TOPO-TA cloning vector (Invitrogen) following manufacturer's protocol.

Reagents and antibodies:

All sources for key reagents are listed in the *Resource Table* above. Unless otherwise mentioned, all chemicals were purchased from Sigma (St Louis, MO). A mouse mAb against the active conformation of Gαi was obtained from Dr. Graeme Milligan (University of Glasgow, UK). Rabbit anti-Arf1 IgG was prepared as described [109]. Rabbit polyclonal anti-α-mannosidase II (Man II) serum was prepared as described [110]. Highly cross-absorbed Alexa Fluor 594 or 488 $F(ab)'_2$ fragments of goat anti-mouse or anti-rabbit IgG (H+L) for immunofluorescence were purchased from Invitrogen (Carlsbad, CA). Goat anti-rabbit and anti-mouse Alexa Fluor 680 or IRDye 800 $F(ab)'_2$ for immunoblotting, were obtained from LI-COR Biosciences.

Cell culture, transfection, ligand stimulation and lysis:

HeLa and MDA MB-231 (American Type Culture Collection, Manassas, VA) were maintained in DMEM (Invitrogen) supplemented with 10% FBS (Hyclone, Logan, UT), 100 U/ml penicillin, 100 µg/ml streptomycin, 1% L-glutamine and 5% CO2. Control and GIV shRNA HeLa and Cos7 stable cell lines were selected with 2 µg/ml of Puromycin (GIBCO) using plasmid expressing a shRNA targeting its 3' UTR [124]. Depletion of GIV was verified using GIV-CT antibody with an efficiency of ~95% and cells were extensively validated in prior studies [18,112,113]. Transfection of cells with fluorescent plasmids (FRET studies) was carried out using transit-LT1 (Mirus Bio, Madison, WI) following the manufacturer's protocol.

For ligand stimulation of cells, serum starvation was carried out overnight (~16-18 h) by replacing media with 0.2% FBS containing media in the case of HeLa prior to exposing them to the ligands.

Lysates used as a source of proteins in pulldown assays were prepared by resuspending cells in Tx-100 lysis buffer [20 mM HEPES, pH 7.2, 5 mM Mg-acetate, 125 mM K-acetate, 0.4% Triton X-100, 1 mM DTT, supplemented with sodium orthovanadate (500 mM), phosphatase (Sigma) and protease (Roche) inhibitor cocktails], after which they were passed through a 28G needle at 4˚C, and cleared (10,000 x g for 10 min) before use in subsequent experiments.

Arf1 activation assays:

Purification of GST-GAT protein and assessment of Arf1 activation were described previously [125]. In brief, cells were lysed with 1% Triton X-100, 50 mM Tris, pH 7.5, 100 mM NaCl, 2 mM $MgCl_2$, 0.1% SDS, 0.5% sodium deoxycholate, 10% glycerol with protease inhibitors. Equal amounts of lysates were incubated with GST-GGA3 (~40 μg) prebound glutathione-Sepharose 4B beads at 4°C for 1 h. Beads were washed, and the bound proteins were eluted by boiling in Laemmli sample buffer for 5 min, resolved on a 15% SDS-PAGE, and analyzed by immunoblotting.

Quantitative immunoblotting:

For immunoblotting, protein samples were boiled in Laemmli sample buffer, separated by SDS-PAGE and transferred onto 0.4 □m PVDF membrane (Millipore) prior to blotting. The duration of transfer was 30 min, at 100 V. Post transfer, membranes were blocked using 5% Non-fat milk or 5% BSA dissolved in PBS. Primary antibodies were prepared in blocking buffer containing 0.1% Tween-20 and incubated with blots, rocking overnight at 4□C. After incubation, blots were incubated with secondary antibodies for one hour at room temperature, washed, and imaged using a dual-color Li-Cor Odyssey imaging system.

Immunofluorescence and confocal microscopy:

For immunofluorescence, cells grown on coverslips were fixed in 3% paraformaldehyde (PFA) and processed as described previously [126]. Antibody dilutions were as follows: Man II, 1:800; anti-Gαi•GTP, 1:25; goat anti-mouse or anti-rabbit Alexa 488 or Alexa 594, 1:500. DAPI was used at 1:10,000. To estimate the degree of colocalization (Mander's overlap coefficient; MOC) [127] in immunofluorescence assays, an ImageJ plugin, JACoP (https://imagej.nih.gov/ij/plugins/track/jacop2.html) was used. This was preferred over Pearson's because it is a good indicator of the proportion of the green signal (active G protein) coincident with a signal in the red channel (Man II, indicative of Golgi membranes) over its total intensity, which may even apply if the intensities in both channels are really different from one another. Coverslips were mounted using Prolong Gold (Invitrogen) and imaged using a Leica SPE CTR4000 confocal microscope.

Image processing: All images were processed on ImageJ software (NIH) and assembled into figure panels using Photoshop and Illustrator (Adobe Creative Cloud). All graphs were generated using GraphPad Prism.

Förster Resonance Energy Transfer (FRET) studies:

Intramolecular FRET was detected by sensitized emission using the three-cube method were performed as previously reported by Midde et al [128]. Briefly, previously validated internally tagged $G\alpha i_1$-YFP and CFP-$G\beta_1$ FRET probe pairs were used [114,115]. All fluorescence microscopy assays were performed on single cells in mesoscopic regime to avoid inhomogeneities from samples as shown previously by Midde et al. [128,129]. Briefly, cells were sparsely split into sterile 35 mm MatTek glass bottom dishes and transfected with 1 µg of indicated constructs. To optimize the signal-to-noise ratio in FRET imaging, various expression levels of the transfected FRET probes were tested. However, to minimize complexities arising from molecular crowding, FRET probes were overexpressed by ~1.5- to twofold compared with the endogenous proteins. Because the stoichiometry of FRET probes has a significant impact on FRET efficiency, cells that expressed equimolar amounts of donor and acceptor probes (as determined by computing the intensity of the fluorescence signal by a photon-counting histogram) were chosen selectively for FRET analyses. An Olympus IX81 FV1000 inverted confocal laser scanning microscope was used for live cell FRET imaging (UCSD-Neuroscience core facility). The microscope is stabilized on a vibration proof platform, caged in temperature controlled (37°C) and CO2 (5%) supplemented chamber. A PlanApo 60x 1.40 N.A. oil immersed objective designed to minimize chromatic aberration and enhance resolution for 405-605 nm imaging was used. Olympus Fluoview inbuilt software was used for data acquisition. A 515 nm Argon-ion laser was used to excite EYFP and a 405 nm laser diode was used to excite ECFP as detailed by Claire Brown's group [130]. Spectral bleed-through coefficients were determined through FRET-imaging of donor-only and acceptor-only samples (i.e. cells expressing a single donor or acceptor FP). Enhanced CFP emission was collected from 425-500 nm and EYFP emission was collected through 535-600 nm and passed through a 50 nm confocal pinhole before being sent to a photomultiplier tube to reject out of plane focused light. Every field of view (FOV) is imaged sequentially through ECFPex/ECFPem, ECFPex/EYFPem and EYFPex/EYFPem (3 excitation and emission combinations) and saved as donor, FRET and acceptor image files through an inbuilt wizard. To obtain the FRET images and efficiency of energy transfer values a RiFRET plugin in Image J software was used [131]. Prior to FRET calculations, all images were first corrected for uneven illumination, registered, and background-subtracted. For FRET quantification, regions of interest (ROI) were drawn in the juxtanuclear area presumably in the Golgi region (or at the cell periphery, presumed to be the plasma membrane regions) to compute energy transfer. Individual cells with fluorescence intensity in the mesoscopic regime detected in the donor and acceptor channels were selected for FRET analysis to avoid inhomogeneities between samples [132,133]

Manual and automatic registration of each individual channel in ImageJ was critical to correct for motion artifacts associated with live cell imaging. Controls were performed in which images were obtained in different orders. The order in which images were obtained had no effect. FRET images were obtained by pixel-by-pixel

ratiometric intensity method and efficiency of transfer was calculated by the ratio of intensity in transfer channel to the quenched (corrected) intensity in the donor channel. The following corrections were applied to all FOVs imaged: For cross-talk correction, cells transfected with CFP or YFP alone were imaged under all three previously mentioned excitation and emission combinations. FRET efficiency was quantified from 3-4 Regions of Interests (ROI) per cell drawn exclusively along the P.M. Because expression of FRET probes may have a significant impact on FRET efficiency, cells that expressed similar amounts of probes, as determined by computing the fluorescence signal/intensity by a photon counting histogram were selectively chosen for FRET analyses. Furthermore, untransfected cells and a field of view with-out cells were imaged to correct for background, autofluorescence and light scattering. To avoid artifacts of photobleaching, Oxyfluor (www.oxyrase.com) was used to minimize the formation of reactive oxygen species.

GFP-tsO45-VSVG transport assays:

To monitor anterograde (ER to Golgi) trafficking control or GIV-depleted COS7 cells were transiently transfected with GFP-tsO45-VSV-G plasmid [134]. Transfected cells were incubated for 14–16 h at the restrictive temperature (40°C) to accumulate VSV-G protein in the ER, shifted to 32°C for 0-60 min to release VSV-G protein in the conditions described (i.e., 10% serum, EGF, or starved condition) and then fixed and processed under non-permeabilized conditions (without detergent) for immunofluorescence. The rate of VSV-G trafficking from the secretory compartments to the PM was determined by calculating the ratio of VSV-G that was already at the PM (as determined using an anti-VSV-G ectodomain antibody; red pixels) normalized to the total cellular pool of VSV-G (GFP; green pixels, using NIH *ImageJ* software.

Metalloprotease and collagen secretion assays:

HeLa cells grown in a 6 well plate was transfected with 2 ug of GFP-MMP2, GFP-MMP9 or Collagen-RFP for 5h. After 5 h, cells were fed with fresh media without FBS. Media was subsequently changed the next day (without FBS; exactly 1.5 ml/well) and stimulated with EGF. Media (100 ul) was collected just before the addition of EGF, as T= 0 h, and at the indicated time points after EGF stimulation. Each aliquot was subjected to high speed (14,000 x g) spin for 10 min prior to the addition of 50 ul of Laemmli sample buffer and boiling at 100℃.

MTT assay:

Cell proliferation was measured using the MTT reagent and cells cultured in 96-well plates. Parental or GIV-KO HeLaor MDA-MB-231 cells were cultured in different concentrations of Fetal Bovine Serum (FBS; 0, 0.25, 2, 5, and 10 %)Then the cell lines were incubated with MTT for 4 hr at 37°C. After incubation, culture media was removed and 150 µl of DMSO was added in order to solubilize the MTT formazan crystals. Optical density was determined at 590 nm using a TECAN plate reader. At least three independent experiments were performed. In an independent experiment we tested the effect of using a Brefeldin A (BFA), a well-known tool to inhibit

secretion, on the cell proliferation. The cell lines were cultured in different concentrations of FBS (0, 0.25, 2, 5, or 10 %) and then treated with different concentrations of BFA (0, 0.01, 0.05, 0.1, 0.5, 1, 10, or 100 μM) and the MTT assays were done as described.

Cell cycle and apoptosis analyses:

Cell cycle analysis and apoptotic cell quantification was performed using the Guava cell cycle reagent (Millipore Sigma) or the annexin V/propidium iodide (PI) staining kit (Thermo Fisher Scientific), respectively, according to the manufacturer's instructions. Cells were quantified on a BD™ (BD Biosciences) LSR II flow cytometer and analyzed using FlowJo software (FlowJo, Ashland, OR, USA).

QUANTIFICATION AND STATISTICAL ANALYSIS

Statistical analyses in modeling approaches: In the deterministic model, we fitted the dose-response curve by finding the best-fit function with the form $a\frac{x^n}{x^n+K}+d$. We solved this optimal problem using 'lsqcurvefit' in Matlab, and d can be deleted depending on the effect of the fitting. The only exception is for the mG versus mGEF, where we used linear function $ax+d$. The difference between the fitted curve and the original curve is measured by R^2, and it is defined as $1-\frac{\sum_i(y_i-f_i)^n}{\sum_i(y_i-\bar{y})^n}$, where y_i is the point in the original curve and f_i is the prediction for y_i based on the best-fit curve. In the stochastic model, the standard deviation is calculated based on the data at 1440min, which is defined as the

$$\sqrt{\frac{\sum_{i=1}^{N}(x_i-\bar{x})^2}{N-1}},$$

where $N=1000$ and $\bar{x}=\frac{\sum_{i=1}^{N}x_i}{N}$. The x_i is the molecular activation or the cell number at 1440min in the i-th simulation.

Statistical analyses in protein-protein network analyses: An interaction cutoff score has been optimized while fetching the new proteins and their interactions from STRING database, such that all the possible proteins will be included keeping the cutoff very high. In this instance, an interaction cutoff score of 667 has been used to include all the proteins from the seed list (**Supplemental dataset 1**).

Statistical analyses in experimental studies and replications: All experiments were repeated at least three times, and results were presented either as one representative experiment or as average ± S.E.M. Statistical significance was assessed with unpaired Student's t test. For all tests, a p-value of 0.05 was used as the cutoff to determine significance. The actual p-values are indicated in each figure. All statistical analysis was performed using GraphPad prism 8 or Matlab.

Supplemental Movie 1 [Related to Fig 2 and Fig S1]

Dynamics within the endomembrane GTPase system. A movie gif that captures the dynamic nature of a circuitry of two species of coupled GTPases, mGTPases (mG) and heterotrimeric GTPases (tG), that is localized on membranes within the secretory pathway.

Supplemental Dataset 2 [Related to Fig 5 and Fig S3]

Excel sheet displays the list of proteins identified as part of the Golgi-localized Arf1-GIV interactome and was used as 'seed' list for creating the Golgi localized protein-protein interaction network.

SUPPLEMENTAL ONLINE MATERIALS

A Eukaryotic Circuit for Secrete-and-Sense Autonomy

Lingxia Qiao[1†], Amer Ali Abd El-Hafeez[2†¶], I-Chung Lo[2†], Saptarshi Sinha[2], Krishna K. Midde[2], Tony Ngo[3], Nicolas Aznar[2], Inmaculada Lopez-Sanchez[2], Vijay Gupta[2], Marilyn G. Farquhar[2€], Padmini Rangamani[1*] and Pradipta Ghosh[2, 4-6*]

Affiliations:
[1]Department of Mechanical and Aerospace Engineering, Jacob's School of Engineering, University of California San Diego, La Jolla, CA.
[2]Department of Cellular and Molecular Medicine, School of Medicine, University of California San Diego, La Jolla, CA.
[3]Skaggs School of Pharmacy and Pharmaceutical Science, University of California San Diego, La Jolla, CA.
[4]Moores Comprehensive Cancer Center, University of California San Diego.
[5]Department of Medicine, School of Medicine, University of California San Diego, La Jolla, CA.
[6]Veterans Affairs Medical Center, La Jolla, CA.

[†]These authors contributed equally.
[€]Acknowledged posthumously

***Correspondence to:**

Padmini Rangamani, Ph.D.; Professor, Department of Mechanical and Aerospace Engineering, University of California San Diego; 9500 Gilman Drive (MC0411), La Jolla, CA 92093.
Phone: 858-534-4734. Email: prangamani@ucsd.edu

Pradipta Ghosh, M.D.; Professor, Departments of Medicine and Cellular and Molecular Medicine, University of California San Diego; 9500 Gilman Drive (MC 0651), George E. Palade Bldg, Rm 232, 239; La Jolla, CA 92093. Phone: 858-822-7633. Email: prghosh@ucsd.edu

¶ **Secondary Affiliation**: Pharmacology and Experimental Oncology Unit, Cancer Biology Department, National Cancer Institute, Cairo University, Cairo, Egypt

SUPPLEMENTAL INFORMATION

INVENTORY OF SUPPLEMENTARY MATERIALS

- **SUPPLEMENTARY TABLES (1)**
- **SUPPLEMENTARY FIGURES AND LEGENDS (6)**

SUPPLEMENTARY TABLES

Supplementary Table 1: Parameter values in the deterministic model

Parameters	values
$stimulus$	0 for serum-starved condition and 0.23 for 50 nM EGFstimulation
(EC_{50}, n) in $f_{act}^{(i)}$, $i = 1, 2, 3, 4, 5, 8$	$(0.5, 1.4)$
(EC_{50}, n) in $f_{act}^{(6)}$	$(0.5, 5)$
(EC_{50}, n) in $f_{act}^{(7)}$	$(0.3, 5)$
(EC_{50}, n) in $f_{act}^{(9)}$	$(0.15, 1.4)$
k_i, $i = tGEF, mG^*$	0
k_{mGEF}	0.008
k_{mGAP}	0.014
k_{tG^*}	0.01
k_S	0.105
β	100 molecules per cell per minute
α	100 molecules per cell per minute
γ	1.67×10^{-2} min^{-1}
K_2	0.3 molecules per μm^3
λ	1.67×10^{-3} min^{-1}
μ	1.67×10^{-4} min^{-1}
K_1	0.25 molecules per μm^3
K	10^{-3} cells per μm^3
Y_i, $i = mGEF, mGAP, mG^*, tG^*$	1
Y_{tGEF}	1 for control cells and 0.1 for GIV-depleted cells
τ_{mGEF}	0.25 min
τ_{mGAP}	15 min
τ_{mG^*}	0.35 min
τ_{tGEF}	0.01 min
τ_{tG^*}	15 min

SUPPLEMENTARY FIGURES AND LEGENDS

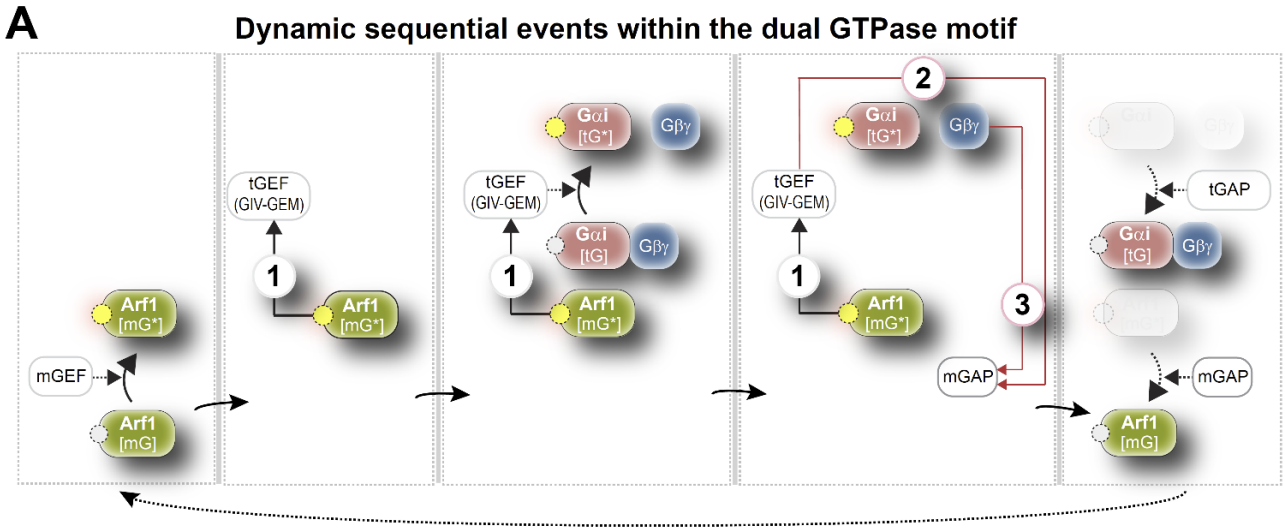

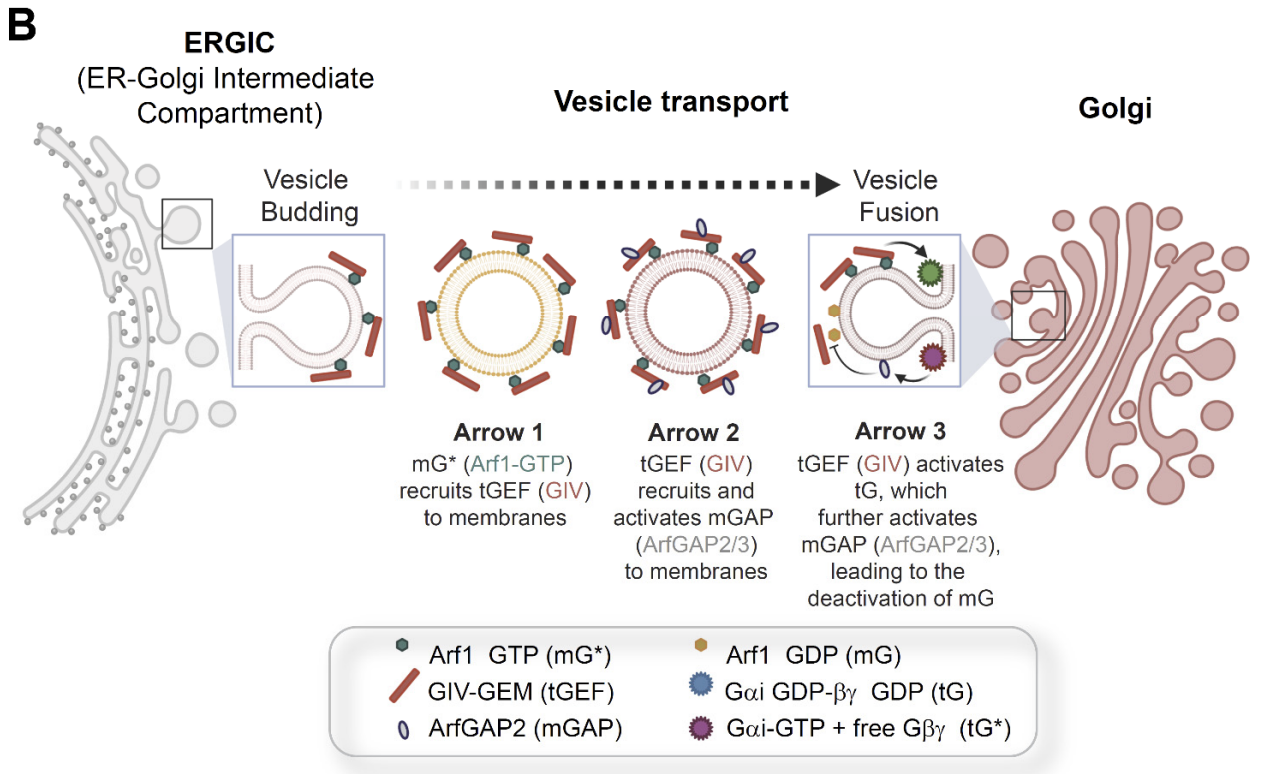

Supplementary Figure 1 (related to Figure 1)

An endomembrane network motif of two species of GTPases regulates membrane trafficking through the secretory pathway, regulates Golgi functions.

A. Dynamics within the endomembrane GTPase system. Left to right panels display the deconstructed Arrows denote key molecular events/chemical reaction cascades within this system, in which, the GIV-GEM links monomeric (m) and trimeric (t) GTPase systems and enable the conversion of extracellular stimuli (ligand; left) into membrane trafficking events (e.g., vesicle uncoating/budding/fusion; right). The feed-forward and feedback reactions (arrows) are numbers 1-3. See **Supplemental Information 1** for a gif of the circuit.

B. Schematic summarizing the findings reported by Lo. I., et al., (Lo et al., 2015) delineating how arrows 1-3 within the endomembrane GTPase system regulates finiteness of Arf1 signaling for efficient secretion.

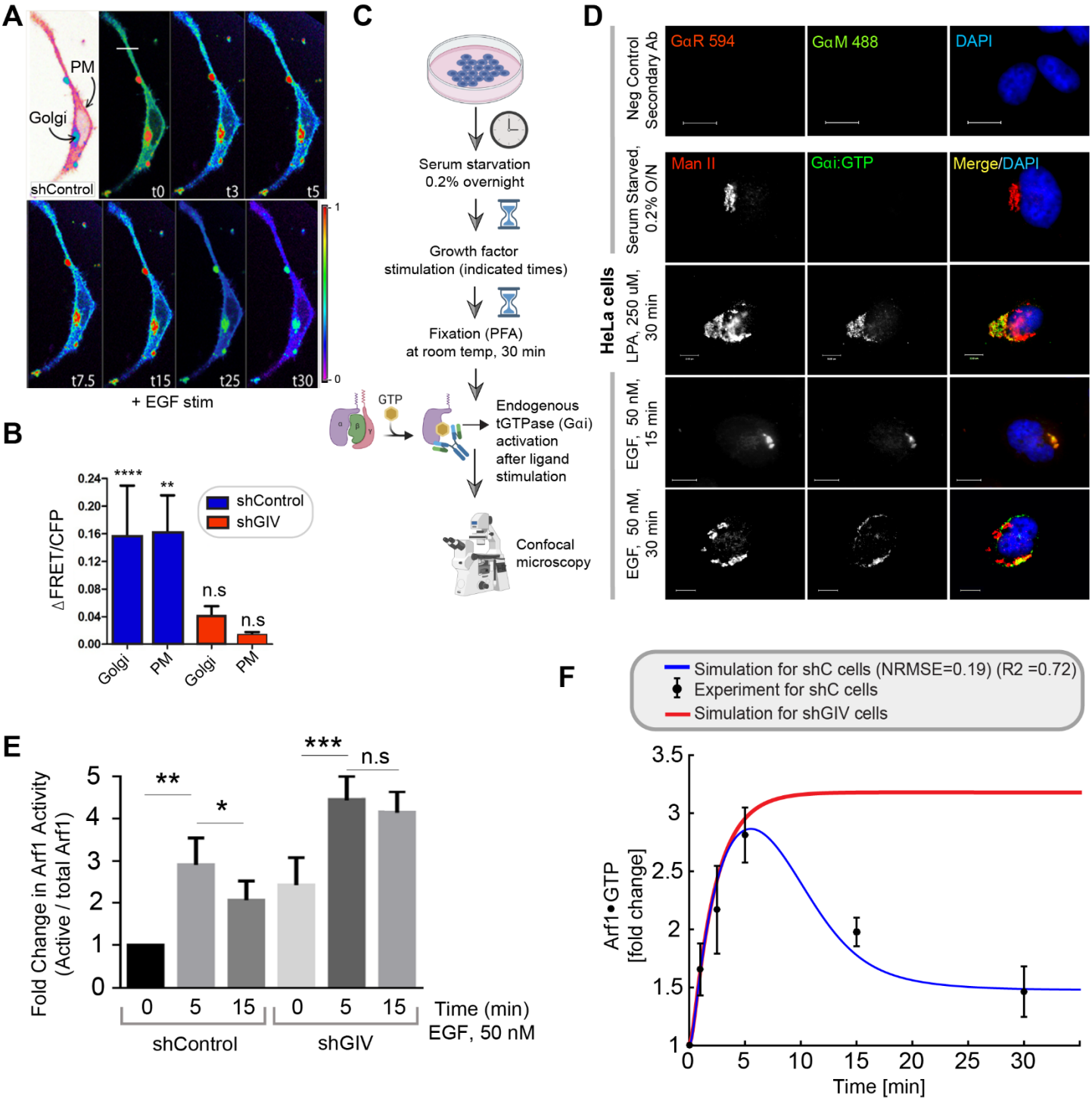

Supplementary Figure 2 (Related to Figure 2).

GEV-GEM is required for Gi activation at the Golgi and for maintaining the finiteness of Arf1 signaling upon EGF stimulation.

A. FRET based studies were carried out in sh Control cells as in **Figure 2B-C**. Briefly, HeLa cells were co-transfected with Gαi1-YFP, Gβ1-CFP and Gγ2 (untagged) and live cells were analyzed by FRET imaging at steady-state, after being serum starved in 0.2% FBS overnight and then after stimulation with 50 nM EGF. Representative freeze-frame FRET images are shown. FRET image panels display intensities of acceptor emission due to efficient energy transfer in each pixel. FRET scale is shown in inset. Golgi and PM regions of interest are indicated with arrows.

B. Bar graphs in I display the change in FRET at t5 min at the Golgi and the PM regions of 3-5 cells, from 4 independent experiments. Scale bar = 7.5 µm. Line graphs in J represent the dynamic change in FRET in the Golgi regions in sh Control vs shGIV cells. Results are displayed as ± S.E.M.

C. Schematic showing how a conformation-specific anti-Gαi•GTP antibody detects GTP-bound active Gαi in situ.

D. HeLa cells starved with 0.2% FBS overnight or stimulated subsequently with 50 nM EGF or 250 μM LPA were fixed and stained for active Gαi (green; anti-Gαi:GTP mAb) and Man II (red) and analyzed by confocal microscopy. Activation of Gαi was detected exclusively after LPA/EGF stimulation. When detected, active Gαi colocalizes with Man II (yellow pixels in merge panel). Negative control (secondary antibody) staining was carried out on cells stimulated with EGF, 15 min. Scale bar = 7.5 μm.

E. Control (sh Control) and GIV-depleted (shGIV) HeLa cells that were stimulated with EGF for the indicated time points prior to lysis were assessed for Arf1 activity. Immunoblots are shown in **Figure 2H**. Bar graphs display the fold change in Arf1 activity normalized to t0 min that was observed in control (shControl) and GIV-depleted (shGIV) cells. Results are expressed as mean ± S.E.M; n = 3 replicates; *p* values were determined using Mann-Whitney t-test compared to t0: *, <0.05; **, <0.01; ***, <0.001. Immunoblots are representative of findings from at least 3 independent repeats.

F. Line graph in red displays model-derived simulation of Arf1 activation dynamics (mG*) in cells without tGEF (shGIV). As reference, results of model-derived simulation fit to experimental data in control cells are displayed in blue.

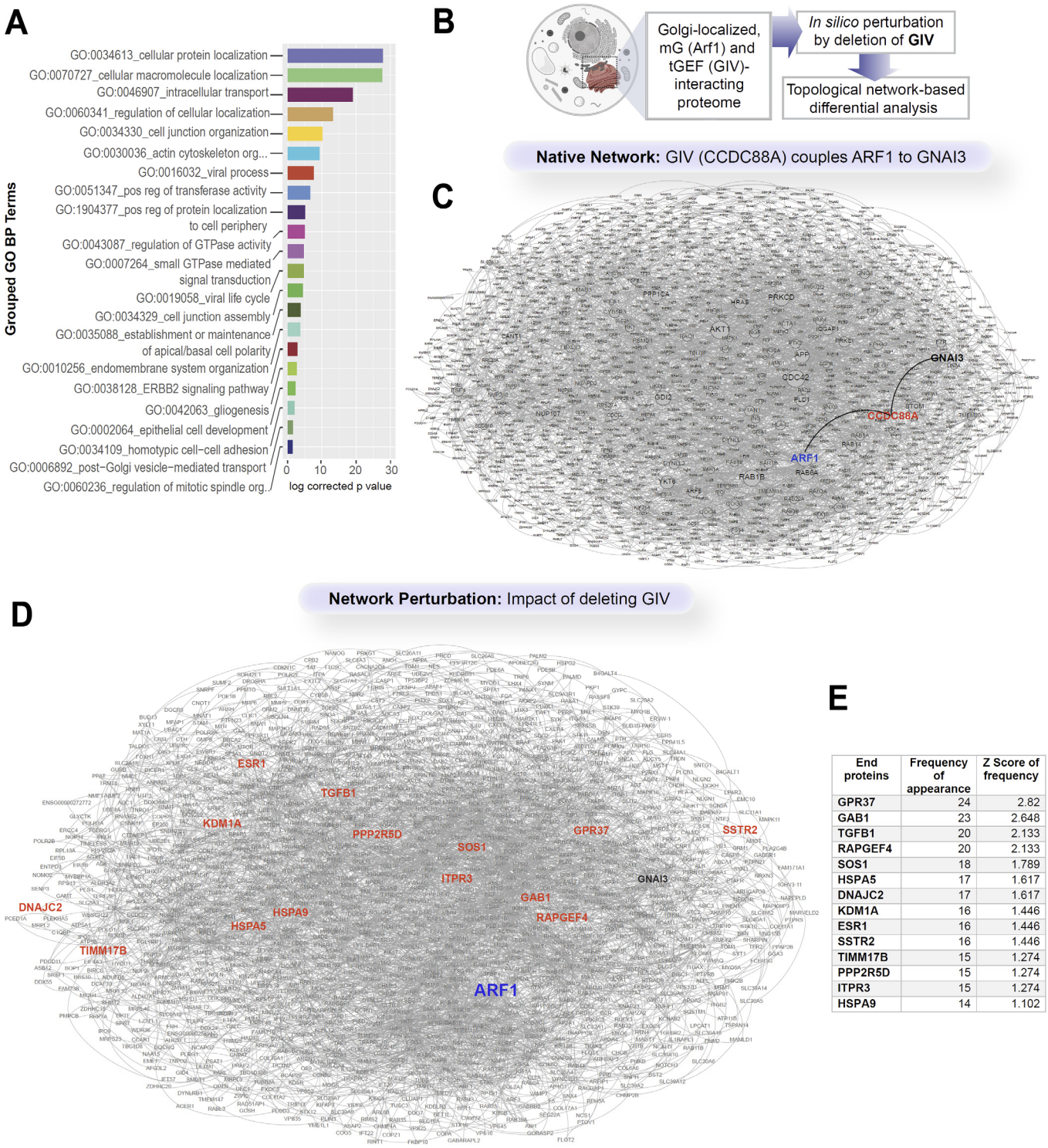

End proteins	Frequency of appearance	Z Score of frequency
GPR37	24	2.82
GAB1	23	2.648
TGFB1	20	2.133
RAPGEF4	20	2.133
SOS1	18	1.789
HSPA5	17	1.617
DNAJC2	17	1.617
KDM1A	16	1.446
ESR1	16	1.446
SSTR2	16	1.446
TIMM17B	15	1.274
PPP2R5D	15	1.274
ITPR3	15	1.274
HSPA9	14	1.102

Supplementary Figure 3 (related to Figure 5)
Protein-Protein Interaction (PPI) network analysis to predict the functions of Golgi-localized coupled GTPases.
A. Gene Ontology biological processes (BP) analysis of a Golgi-specific GIV and Arf1 interaction network. See also **Supplemental dataset 2** for the complete list of proteins.
B. Workflow schematic for PPI network analysis. See also **Fig 5C**.
C. A PPI network created using Golgi specific interactions of Arf1 and GIV fetched from HCM using Golgi specific proteins. Here the diameter of each nodes corresponds to its degree of conectivity within this PPI network. The interactions of GIV that allows it to serve as a linker between Arf1 (mGTPase) and GNAI3 (tGTPase) are highlighted.
D. Consequences of GIV(CCDC88A) deletion on the shortest paths alterations associated with Arf1. The end proteins of the most affected shortest paths have been highlighted in red.
E. Table displays a selected list of end proteins associated with altered shorted paths of Arf1 due to GIV deletion. The proteins are selected based on their frequency of appearance as end proteins in these shortest paths, using a Z score of the frequency >=1 as cut-off.

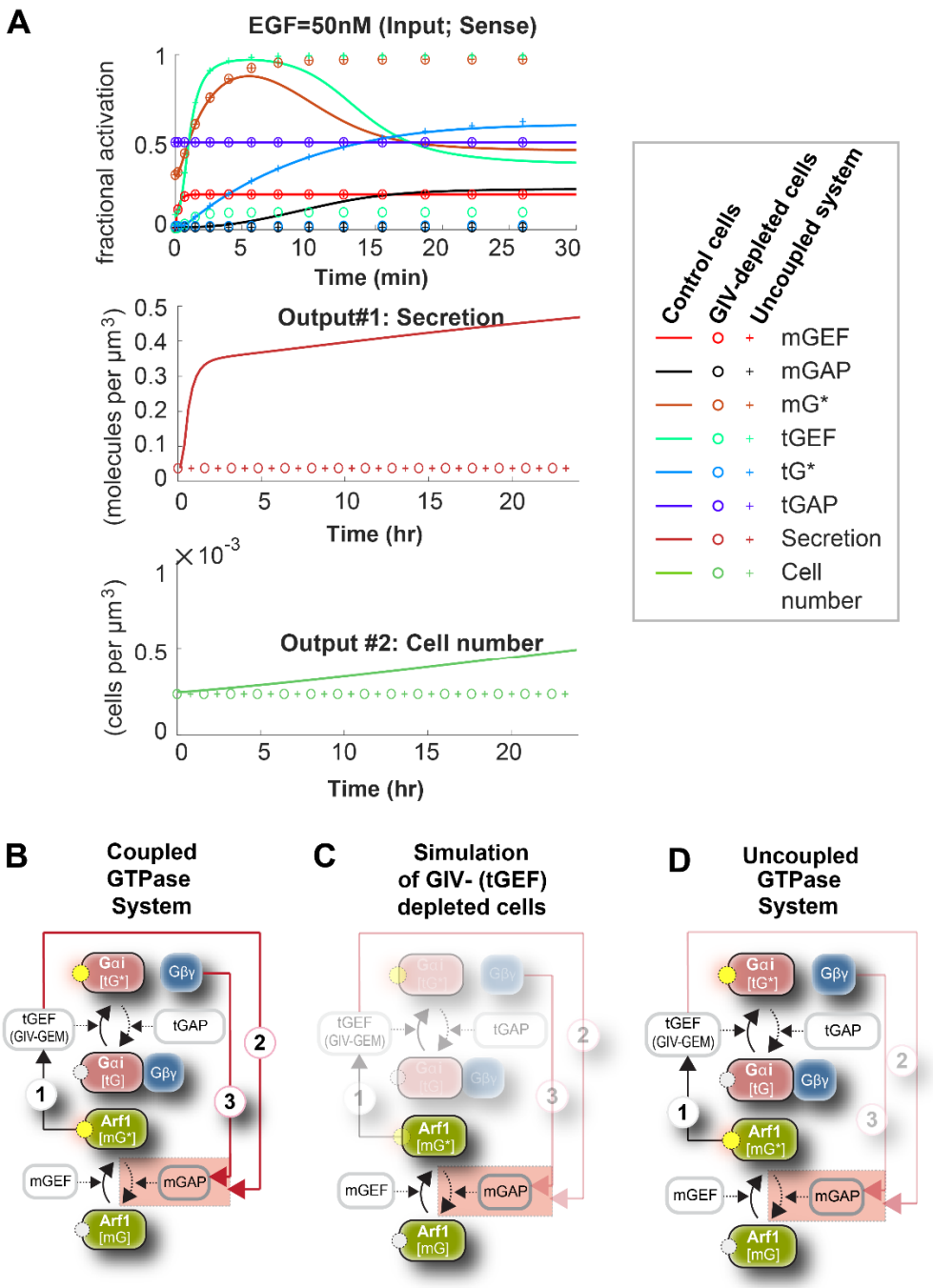

Supplementary Figure 4. (related to Figure 6)

Simulations of secretion and cell number models for control cells (with a fully coupled GTPase system), in GIV-depleted cell (arrows 1-3) and cells with an uncoupled GTPase system (missing feedback control arrows 2 and 3).

A. Model-derived simulation of dynamics for control cells, GIV-depleted cells and the uncoupled system when EGF=50nM. Schematics in **B-D** display these three conditions. The initial condition is the steady state in serum-starved condition except that the cell number is set to be the carrying capacity K. The equations **Error! Reference source not found.**-**Error! Reference source not found.** with parameters in **Supplementary Table 1** are used, and the $stimulus$ changes to 0.23 at time zero.

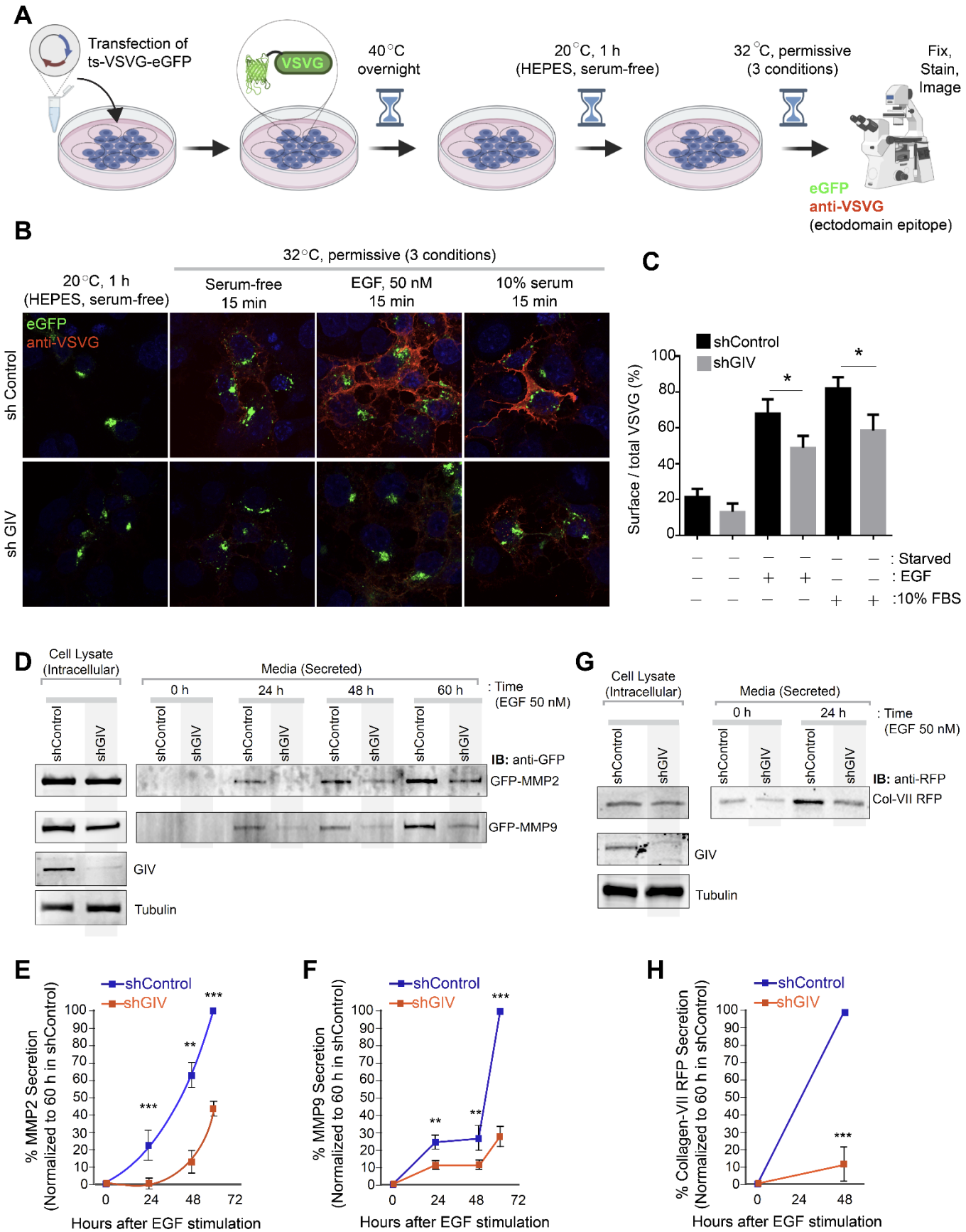

Supplementary Figure 5. (related to Figure 7)

GIV-GEM is required for EGF-triggered secretion of diverse cargo proteins through Golgi compartment.

A. Schematic shows the basis for measuring secretion of transmembrane cargo protein, ts-VSVG-eGFP. This temperature-sensitive mutant VSVG is retained in the ER at 40°C, at the Golgi at 20°C, and moves out of the Golgi to the PM when shifted to 32°C (Gallione and Rose, 1985). When visualized with immunofluorescence under non-permeabilized conditions, a VSVG-ectodomain targeting antibody selectively detects PM-localized cargo, whereas GFP tag allows the visualization of total VSVG in the cell.

B-C. Control (sh Control; top) and GIV-depleted (shGIV; bottom) Cos7 cells were transfected with tsO45-VSVG-GFP and cells were shifted to 40°C for O/N and then incubated at 20°C for 1 h in HEPES buffered serum free media followed by temperature shift at 32°C for 15 minutes in plain DMEM and or containing 50nM EGF or 10% serum. Coverslips were fixed and stained with VSVG-ectodomain specific monoclonal antibody (red). Representative images are shown in B. Green fluorescence indicates total VSVG expression whereas red fluorescence shows surface-localized pool of VSVG. Bar graphs in C display the Red:Green intensity ratio indicative of fraction VSVG that is secreted to the cell surface. Results are expressed as mean ± S.E.M; n = 3 replicates; *p* values were determined using Mann-Whitney t-test compared to t0: *, <0.05.

D-H. Control (sh Control) and GIV-depleted (shGIV) HeLa cells were analyzed for EGF-stimulated secretion of three soluble cargo proteins, MMP2 (D, E), MMP9 (D, F) and Collagen-Vii RFP (G, H), as detected from the supernatants at indicated time points after EGF stimulation. Results are expressed as mean ± S.E.M; n = 3 replicates; *p* values were determined using Mann-Whitney t-test compared to t0: *, <0.05; **, <0.01; ***, <0.001. Immunoblots are representative of findings from at least 3 independent repeats.

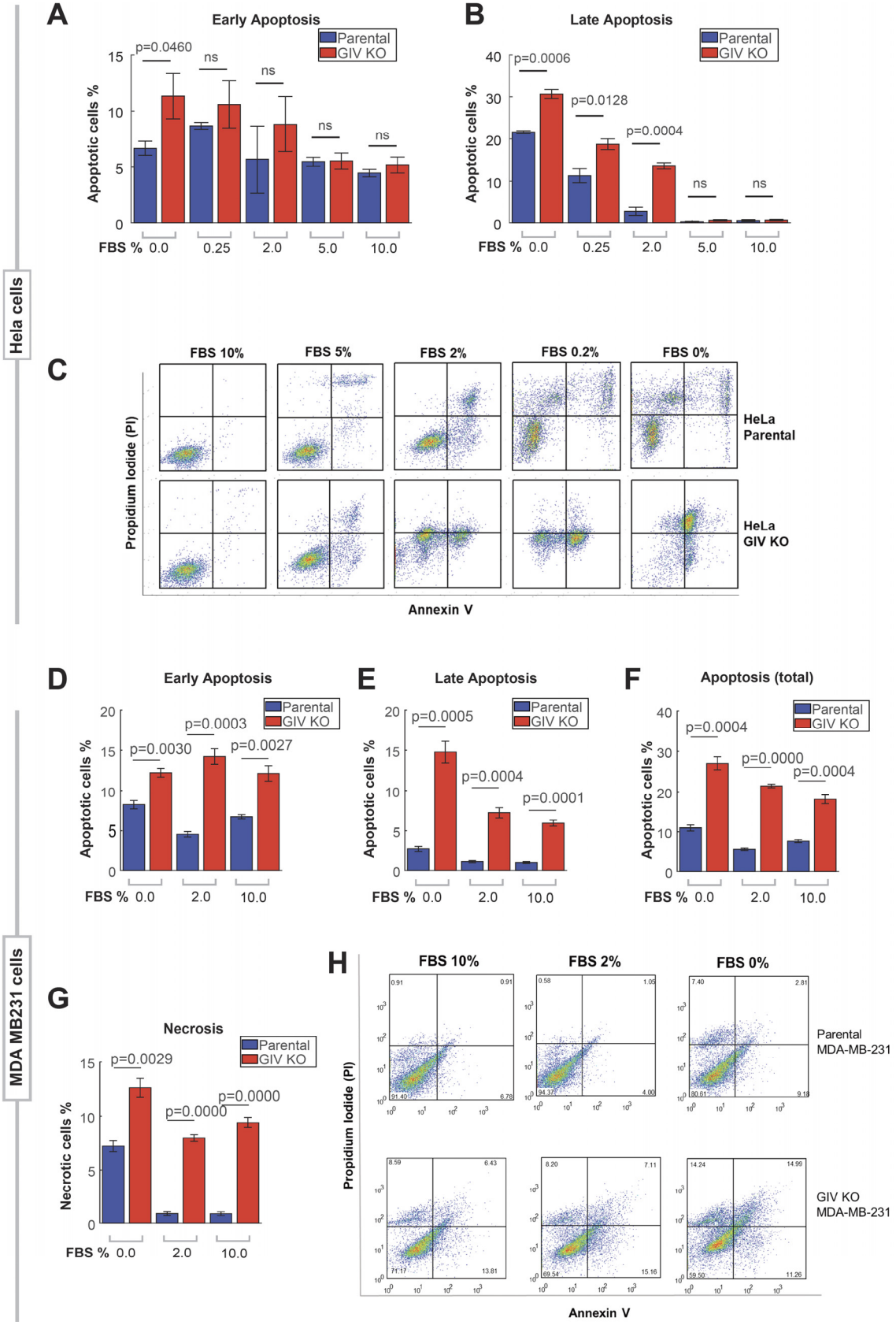

Supplementary Figure 6. (related to Figure 7)

GIV-GEM is required for cell survival. A-C. Bar graphs display the % early (A) or late (B) apoptotic control (parental) and GIV-depleted (GIV KO) HeLa cells after 24 h growth in varying concentration of serum, as assessed by annexin V staining and flow cytometry. The dot plot diagrams are shown in C. **D-H**. Bar graphs display the % early (D), late (E) or total (early + late; F) apoptotic and necrotic (G) control (parental) and GIV-depleted (GIV KO) MDA MB-231 cells after 24 h growth in varying concentration of serum, as assessed by annexin V staining and flow cytometry. The dot plot diagrams are shown in H. Results are expressed as mean ± S.E.M; n = 3. p values were determined by unpaired t-test.

SUPPLEMENTARY BIBLIOGRAPHY

Gallione, C.J., and Rose, J.K. (1985). A single amino acid substitution in a hydrophobic domain causes temperature-sensitive cell-surface transport of a mutant viral glycoprotein. Journal of virology *54*, 374-382.

Lo, I.-C., Gupta, V., Midde, K.K., Taupin, V., Lopez-Sanchez, I., Kufareva, I., Abagyan, R., Randazzo, P.A., Farquhar, M.G., and Ghosh, P. (2015). Activation of Gαi at the Golgi by GIV/Girdin imposes finiteness in Arf1 signaling. Developmental cell *33*, 189-203.